Inorganic Chemistry

pubs.acs.org/IC Article

Model Dimeric Manganese(IV) Complexes Featuring Terminal Tris-hydroxotetraazaadamantane and Various Bridging Ligands

Dejan Premužić, Małgorzata Hołyńska,* Andrew Ozarowski,* Clemens Pietzonka, Alexander Roseborough, and Sebastian A. Stoian*

Cite This: *Inorg. Chem.* 2020, 59, 10768−10784 Read Online

ACCESS | Metrics & More | Article Recommendations | Supporting Information

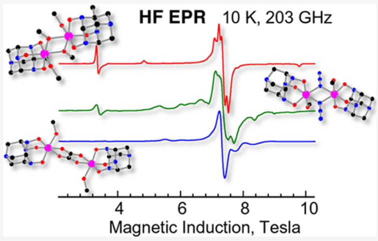

ABSTRACT: A series of model dinuclear manganese(IV) complexes of the general formula $[(H_3COH)(L')Mn^{IV}(\mu\text{-}L)_2Mn^{IV}(L')(HOCH_3)]$ is presented. These compounds feature capping 4,6,10-trihydroxo-3,5,7-trimethyl-1,4,6,10-tetraazaadamantane ligands derived from a polydentate oxime compound (L′). The bridging ligands L include azide (**1**), methoxide (**2**), and oxalate (**3**) anions. The magnetic properties and high-field (HF) EPR spectra of **1**−**3** were studied in detail and revealed varying weak antiferromagnetic coupling and modest zero-field splitting (ZFS) of the local quartet spin sites. Our HF EPR studies provide insight into the dimer ZFS, including determination of the corresponding parameters by giant spin approach for methoxido-bridged complex **2**. Furthermore, the physicochemical properties of **1**−**3** were studied using IR, UV−vis, and electrochemical (cyclic voltammetry) methods. Theoretical exchange coupling constants were obtained using broken-symmetry (BS) density functional theory (DFT). Computational estimates of the local quartet ground spins state ZFSs of **1**−**3** were obtained using coupled-perturbed (CP) DFT and complete active space self-consistent field (CASSCF) calculations with *n*-electron valence state perturbation theory (NEVPT2) corrections. We found that the CP DFT calculations which used the B3LYP functional and models derived experimental structures performed best in reproducing both the magnitude and the sign of the experimental *D* values. Moreover, our computational investigation of **1**−**3** suggests that we observe metals sites which have an increased +3 character and are supported by redox noninnocent 4,6,10-trihydroxo-3,5,7-trimethyl-1,4,6,10-tetraazaadamantane ligands. The latter conclusion is further corroborated by the observation that the free ligand can be readily oxidized to yield a NO-based radical.

■ INTRODUCTION

Metalloenzymes which incorporate high-valent manganese sites are involved in a broad array of biological processes.[1] These range from the reduction of ribonucleotides to deoxynucleotides, during the synthesis of DNA precursors, effected by the dinuclear manganese clusters of class Ib ribonucleotide reductases (Mn-RNR), to the removal of cytotoxic superoxide radicals by the manganese-dependent superoxide dismutase.[2] Undoubtedly, the best-known and most intensely studied biotic manganese cluster is the Mn_4CaO_5 active site of photosystem II used by photosynthetic organisms to oxidize water and evolve molecular oxygen (OEC).[3] While most of these enzymes incorporate high-valent manganese(IV) ions in their catalytic cycles, the exact role of the +4 oxidation state is not always evident. Most often, such species are used to either modulate the reactivity of reactive radical species or to generate new radicals.[4] For example, it has been proposed that the assembly of the $Mn^{III}{}_2Y^{\bullet}$ cofactor of Mn-RNR is initiated by the oxidation of the $Mn^{II}{}_2$ by an $O_2{}^{\bullet-}$ and proceeds through an oxidized $Mn^{III}(\mu\text{-}O)(\mu\text{-}OH)Mn^{IV}$ intermediate.[5] Moreover, the successive oxidation steps of the OEC involve multiple proton-coupled electron transfer steps and a tyrosine radical such that the electronic structure of the cofactor immediately prior to O−O bond formation might be best described as a dimer of $Mn^{IV}{}_2$ dimers.[6] Therefore, the study of coordination compounds which incorporate analogous metal sites supported by redox noninnocent ligands such as organic radicals are of interest as both structural and functional model complexes of manganese enzymes.

Several studies have recently shown that just like their $Fe^{IV}{=}O$ analogues nonheme Mn^{IV}-oxo compounds supported by neutral pentadentate ligands also activate strong C−H bonds.[7,8] It has been suggested that the enhanced hydrogen atom abstraction (HAT) reactivity of these $Mn^{IV}{=}O$ species originate from the synergistic effects of two-level reactivity involving the $^4B_1$ and ^4E levels electronic states, the π-bonding interactions of substrates with the $Mn^{IV}{=}O$ group, and the unusually high redox potential of the $Mn^{III/IV}$ couple.[9] Interestingly, the HAT reactivity was not limited to mononuclear compounds but also observed for some dinuclear complexes.[10] Furthermore, the presence of terminal oxo

Received: April 28, 2020
Published: July 20, 2020

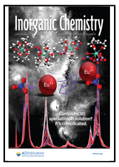

https://dx.doi.org/10.1021/acs.inorgchem.0c01242
Inorg. Chem. 2020, 59, 10768−10784

ligands is not even a prerequisite for manganese(IV) species to exhibit biomimetic catalytic activity.[11] One notable series of such compounds are the radical-supported $Mn^{IV}_2(L^{\bullet})_2(L^{\bullet\bullet})$ and $Mn^{IV}L(L^{\bullet})_2$ where L are *o*-aminophenols derived from aniline and *m*-phenylenediamine, which catalyze the oxidation of catechol to quinone and the oxidative coupling of C−C bonds of hindered phenols using oxygen as the sole oxidant.[12] Since manganese(IV) compounds have the potential of using molecular oxygen as a cheap and plentiful oxidant to effectuate difficult partial oxidation of organic substrates, their studies not only advance our understanding of biological processes but also are likely to lead to applications of great technological importance. Despite of their significance there are only a handful of dinuclear Mn^{IV}_2 compounds for which their magnetic properties were reported. With few exceptions most of these examples are limited to oxo-bridged dimers,[13] such as $[L_2Mn_2(\mu\text{-}O)\mu\text{-}phBO_2)_2](PF_6)_2$ (L = 1,4,7-trimethyl-1,4,7-triazacyclononane, $phBO_2$ = phenyl boronic acid).[14,15] Interestingly, a strong dependence of the metal−metal interaction strength on the protonation of the oxo-bridges was reported.[13c] Although these metals sites are usually probed using X-band EPR spectroscopy, the dimeric molecules exhibit relatively large zero-field splitting in their spin-triplet state requiring application of the HF EPR measurements. In this contribution, we expand the range of known dinuclear Mn^{IV}_2 complexes by describing a series of three new compounds supported by an adamantane-like ligand, 4,6,10-trihydroxo-3,5,7-trimethyl-1,4,6,10-tetraazaadamantane, and three distinct, bridging coligands, see Scheme 1. All three complexes are bridged by non-oxo ligands which is an unusual feature contrary to the majority of the Mn(IV)-based dimers reported to date. The tridentate $L'H_3$ ligand is deprotonated and acts as a stopper, saturating the coordination spheres of the individual manganese ions. Interestingly, this organic molecule is obtained *in situ* through an unusual cyclization of the starting tris(2-hydroxyiminopropyl)amine, Ox_3H_3; see Scheme 2. The coordinating behavior of both Ox_3H_3 and $L'H_3$ have been previously investigated such that some complexes supported by these ligands have been already reported.[16] In addition to its adamantane-like structure, the most unusual feature of the metal-bound $(L')^{3-}$ is that it incorporates three NO^- moieties which, for the free ligand, can be easily oxidized to their $NO^{\bullet}$ paramagnetic, electrically neutral form. Thus, the deprotonated free ligand is easily oxidized to yield an EPR-active radical species. The electronic structure of these new Mn^{IV}_2 compounds was determined through a combined HF EPR, SQUID, and computational investigation which revealed that ligand noninnocence plays an important role in modulating their magnetic properties and ground state electronic configurations.

Scheme 1. Reaction System Leading to the Isolation of 1−3

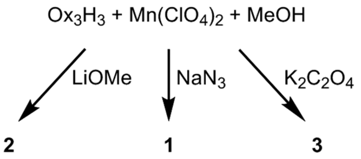

Scheme 2. Intramolecular Cyclization of the Tris(2-hydroxyiminopropyl)amine Ligand Catalyzed by Metal Complexes

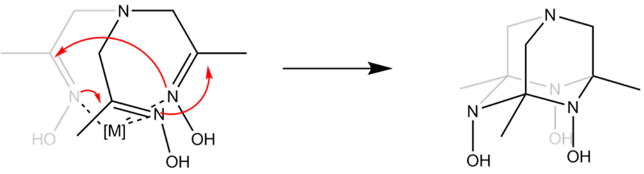

EXPERIMENTAL SECTION

General Information. All reactions were performed under aerobic conditions using HPLC-grade solvents as purchased. The tris(2-hydroxyiminopropyl)amine ligand was obtained with a modified procedure described elsewhere.[17,18] All other reagents were obtained from commercial suppliers and were used without further purification. IR spectra were recorded on a Bruker Alpha-P IR-spectrometer with a Platinum-ATR with a diamond crystal. Elemental analyses were performed with a Vario Microcube elemental analyzer in CHNS mode. UV/vis-spectra were recorded for 0.1 mM solutions in THF on a Varian Cary 5000 UV−vis−NIR Spectrophotometer. Cyclic voltammograms (CVs) were recorded in a platinum vessel with platinum electrodes and an Autolab potentiostat at a scan rate of 200 mVs^{-1} for the characterization of 1−3 and 100 mVs^{-1} for the investigation of the free ligand. DMSO solutions of samples with concentration of 1 mM in the presence of NBu_4PF_6 (0.1 M) were prepared under inert atmosphere. Magnetic measurements were recorded with the Magnetic Property Measurement System (MPMS) made by Quantum Design. The magnetic data were obtained in the temperature range from 2 to 300 K at the fields of 500 and 1000 G. The ground powder samples were sealed in gelatin capsules. The data were corrected for the sample holder contribution and the diamagnetic corrections were calculated using Pascal constants.[19] High-field, high-frequency EPR spectra at temperatures ranging from ca. 3 to 290 K were recorded on a custom-built spectrometer at the EMR facility of the NHMFL.[20] The instrument is equipped with a superconducting magnet (Oxford Instruments) capable of reaching a field of 17 T. Microwave frequencies over the range 52−630 GHz were generated by a phase-locked Virginia Diodes source, producing a base frequency of 13 ± 1 GHz, which was multiplied by a cascade of frequency multipliers. The instrument is a transmission-type device and uses no resonance cavity.

Syntheses. *$[(H_3COH)(L')Mn^{IV}(\mu\text{-}N_3)_2Mn^{IV}(L')(HOCH_3)]$ (**1**).* $Mn(ClO_4)_2\cdot xH_2O$ (254 mg, 1.0 mmol), Ox_3H_3 (230 mg, 1.0 mmol), and sodium azide (325 mg, 5.0 mmol) were combined in 30 mL of methanol. The resulting brown solution was stirred for 1 h, filtered, and left for slow evaporation. After ca. 1 week, crystals of **1** in form of large dark-red blocks were collected at 40% yield (156 mg). Upscaling of the reaction by 10 times increased the yield to 46% (1.80 g). Elemental analysis calcd (found) for $C_{20}H_{38}Mn_2N_{14}O_8$ (M = 712.48): C 33.72 (32.50), H 5.38 (4.85), N 27.52 (27.59). Apparently, a loss of 2 methanol ligands of solvation and weakly coordinated to the Mn^{IV} ions has to be taken into account. IR bands: 3353.0 (w), 2982.8 (w), 2938.6 (w), 2071.6 (s), 1641.2 (w), 1456.7 (w), 1434.7 (w), 1372.6 (w), 1342.2 (w), 1290.8 (w), 1268.9 (w), 1210.2 (w), 1179.2 (w), 1163.1 (w), 1041.5 (s), 979.7 (m), 825.9 (s), 808.6 (s), 754.9 (w), 696.3 (s), 664.0 (w), 626.7 (s), 593.5 (w), 532.2 (s), 487.6 (m), 417.6 (w).

*$[(H_3COH)(L')Mn^{IV}(\mu\text{-}OCH_3)_2Mn^{IV}(L')(HOCH_3)]$ (**2**).* $Mn(ClO_4)_2\cdot xH_2O$ (254 mg, 1.0 mmol), Ox_3H_3 (230 mg, 1.0 mmol), and lithium methoxide (38 mg, 1.0 mmol) were combined in 30 mL of methanol. The resulting brown solution was stirred for 1 h, filtered and left for slow evaporation. After ca. 1 week crystals of **2** in form of large dark-red blocks were collected at 46% yield (160 mg). Upscaling of the reaction by ten times increases the yield to 54% (1.86 g). Elemental analysis calcd (found) for $C_{22}H_{44}Mn_2N_8O_{10}$ (M= 690.51): C 38.27 (37.75), H 6.42 (6.44), N 16.23 (15.95). IR bands: 3645.5 (w), 3439.2 (w), 3015.4 (w), 2975.4 (w), 2934.3 (w), 2807.9 (w), 1625.0 (w), 1455.8 (w), 1427.7 (w), 1371.4 (w), 1326.6 (w), 1264.7 (w), 1205.7 (w), 1179.3 (w), 1163.9 (w), 1041.6 (s), 1010.2 (m), 975.5

(m), 815.3 (s), 699.0 (s), 655.6 (w), 626.2 (s), 585.3 (w), 523.3 (s), 505.3 (s), 452.7 (m), 419.2 (w).

[(H_3COH)(L′)Mn^{IV}(μ-ox)Mn^{IV}(L′)($HOCH_3$)] **(3).** $Mn(ClO_4)_2 \cdot xH_2O$ (254 mg, 1.0 mmol), Ox_3H_3 (230 mg, 1.0 mmol), and potassium oxalate monohydrate (92 mg, 0.5 mmol) were combined in 30 mL of methanol. The resulting brown solution was stirred for 1 h, filtered and left for slow evaporation. After 2 days, a colorless precipitate was formed, the solution was filtered and left for slow evaporation. After ∼1 week, crystals of **3** in form of dark-red plates accompanied by potassium perchlorate (identified by measurement of the cell constants) were collected. After mechanical separation of the product from potassium perchlorate a yield of 17% (65 mg) is achieved. Elemental analysis calcd (found) for for $C_{24}H_{46}Mn_2N_8O_{14}$ (M = 780.54): C 36.93 (35.10), H 5.94 (5.68), N 14.36 (14.37) (the discrepancies were caused by the small amount of $KClO_4$ impurity). IR bands: 3438.1 (w), 2986.3 (w), 2942.3 (w), 1633.2 (s), 1460.8 (w), 1428.6 (w), 1375.9 (w), 1350.8 (w), 1330.2 (w), 1307.7 (w), 1269.4 (w), 1212.5 (w), 1180.2 (w), 1044.1 (s), 1019.5 (m), 978.9 (w), 827.6 (s), 802.6 (s), 757.7 (w), 698.6 (m), 626.7 (m), 531.1 (s), 481.7 (m), 405.4 (w).

X-ray Diffraction. X-ray diffraction data for single-crystals of **1**, **2**, and **3** were collected on a STOE IPDSII diffractometer, employing Mo Kα radiation (see Table S1 for selected X-ray data).

Details of Structure Refinement. All structures were solved by direct methods in SHELXS and refined in SHELXL software.[21] C-bonded H atoms were placed in their calculated positions and treated with a riding model with U_{eq} = 1.2/1.5 U_{eq} (parent C atom). O-bonded H atoms positions were found on difference Fourier maps and initially refined with DFIX restraints setting the O−H bond lengths at 0.840(2) Å. Subsequently, these H atom positions were constrained. On the final difference Fourier map, the highest peak of 0.38 e/Å^3 is located 0.80 Å from the O13 atom (1.09 Å from the Mn1 atom)/0.36 e/Å^3 at 1.06 Å from the Mn1 atom/0.75 e/Å^3 at 0.85 Å from the Mn1 atom for **1**, **2**, and **3**, respectively.

Theoretical Methods. The electronic structure calculations of **1**−**3** were performed using the Gaussian[22] and ORCA[23] quantum mechanical software packages. DFT calculations used the spin-unrestricted formalism and the B3LYP, BP86, and TPSSH functionals in combination with 6-311G, 6-311G*, 6-311+G**, and TZVP-SVP basis sets. Geometry optimized structure were obtained, using Gaussian 09, at each of the B3LYP, BP86, TPSSH/6-311G, 6-311G*, and 6-311+G** levels of theory. These calculations employed simplified structural models for which the three methyl groups of the 4,6,10-trihydroxo-3,5,7-trimethyl-1,4,6,10-tetraazaadamantane ligands were replaced with hydrogen atoms. Optimized structures were obtained not only for the ferromagnetic (F, S = 3) states but also for the broken-symmetry (BS, S = 0) states, *vide infra*. Single-point calculations were used to assess the nature of the ground state configurations and to obtain predicted properties, single-electron excitations using time-dependent (TD) DFT, predicted atomic charges, and atomic spin densities using Mulliken population analysis, natural populations of the valence shells using Natural Bond Orbitals (NBO 3.0) analysis, and exchange coupling constants. These calculations were performed using both unabridged structural models derived from the experimental X-ray coordinates and geometry-optimized simplified structural models; see Table S21. Geometry optimizations and single-point SCF calculations were completed using the default convergence criteria. The theoretical exchange coupling constants were obtained using a broken symmetry approach.[24−29] While the B3LYP, BP86, TPSSH/6-311G, 6-311G*, and 6-311+G** values were obtained using the Gaussian 09 program, the B3LYP/TZVP results were obtained using ORCA.[30−38] These values were determined by taking the difference of the SCF energies predicted for the ferromagnetic (S = 3) and broken-symmetry (S = 0) states. The BS state corresponds to configurations for which three unpaired spin-up, α electrons localized on one site and three unpaired spin-down, β electrons localized on the other site. The J values (using the $\hat{H}_{exchange} = -2J\hat{S}_1 \cdot \hat{S}_2$ formalism) were evaluated by means of the $J = -(\varepsilon_F - \varepsilon_{BS})/(\langle \hat{S}^2 \rangle_F - \langle \hat{S}^2 \rangle_{BS})$ expression, where ε are the energies and $\langle \hat{S}^2 \rangle$ are the average values of the total spin-squared operator of the ferromagnetic and BS states. For local quartet states this expression yields $J = -(\varepsilon_F - \varepsilon_{BS})/9$.

The theoretical ZFS parameters of the local quartet ground states were obtained using the coupled-perturbed (CP) DFT and the state-averaged CASSCF/NEVPT2 methods as implemented in the ORCA suite of programs.[39−41] The CP DFT calculations employed the BP86, B3LYP, TPSSH functionals, Pople's 6-311G, 6-311G*, and 6-311+G** basis sets, and were performed on mononuclear models. These computational models were obtained by deleting a $[MnAd]^+$ moiety from either the experimental or from the geometry-optimized structures obtained using the respective functional/basis set or from the experimental structures. The CASSCF/NEVPT2 calculations used mononuclear structural models derived from the simplified B3LYP/6-311G geometry-optimized structures of the F states and experimental structures for which one of the $[L'Mn]^+$ moieties were deleted. The CASSCF/NEVPT calculations used the diffuse def2-TZVPP basis set and the def2/JK the auxiliary basis set (the RI-JK approximation was used).[42,43] The quasi-restricted orbitals used to set up the initial guesses of the CASSCF(3,5) calculations were obtained by performing single-point DFT(BP86) calculations. In this case the active space consisted of only the 3d metal ions of the Mn(IV) sites. The CASSCF(7,7) calculations were used as initial guesses for the converged CASSCF(3,5) calculations (CASSCF(11,9) used CASSCF(7,7)). Utilizing as a starting point the active space of CASSCF(3,5), the active space of CASSCF(7,7) was expanded to also included the ligand-based, sigma-bonding e_g-type orbitals and, for the CASSCF(11,9), the π^*_{NO}-based orbitals. Regardless of the dimension of the active space, 10 quartet and 9 doublet roots were calculated. To ensure that the desired active space was selected, when needed, the *rotate* option of the *scf* ORCA keyword was used.

■ RESULTS AND DISCUSSION

Formation. The title series of complexes were isolated from a system summarized in Scheme 1. The tridentate Ox_3H_3 and $Mn(ClO_4)_2$ were combined in methanol with an appropriate salt. Interestingly, from this system only Mn^{IV} complexes could be isolated so far.

It was shown that the Ox_3H_3 ligand may undergo an intramolecular cyclization to yield a 1,4,6,10-tetraazaadamantane derivative $L'H_3$ (Scheme 2) isomeric to 1,3,5,7-tetraazaadamantane (urotropin). This process is catalyzed by metal ions, such as Co^{II}, which upon coordination bring the three oxime groups closer together.[17] Apparently in our system, a similar cyclization takes place, accompanied by oxidation of the starting Mn^{II} ions to Mn^{IV}. In similar systems with oxime ligands, Mn^{II} salts, and under basic conditions, the usual products are Mn^{III} complexes. The unique stabilization of Mn^{IV} in our case seems to be related to the use of the tetraazadamantane ligand.

When the tetraazadamantane ligand was first synthesized using a previously reported method[17] and directly used as a starting material, the reactions with the Mn ions ran faster. However, for **1** and **2** the products were not crystalline, and for **3** the yield was much lower. This behavior indicates that the first step in the formation of **1**, **2**, and **3** is the slow cyclization of Ox_3H_3 to the 4,6,10-trihydroxo-3,5,7-trimethyl-1,4,6,10-tetraazaadamantane ligand.

Optimization of the reaction conditions was carried out by varying the amount of the bridging ligand, while the $Mn(ClO_4)_2/Ox_3H_3$ ratio was kept at 1:1. In the case of **1**, an excess of NaN_3 (up to 6 equiv) was used. The best yield was achieved with 5 equiv. Increasing the temperature had no effect on the yield; therefore, all reactions were carried out at room temperature. For **2**, various methoxide salts were used, ranging from LiOMe to NaOMe and $Ca(OMe)_2$, but no differences in the yield and quality of the crystalline products were observed.

Also, the use of other bases like NaOH yields **2**. In the case of **3**, many different oxalate-salts like Li_2Ox, $(NH_4)_2Ox$, Na_2Ox, and K_2Ox (Ox, oxalate) were used, but only in the case of K_2Ox is **3** obtained as a crystalline product, accompanied with a colorless precipitate identified as $KClO_4$. **3** crystallized as small intergrown plates which were separated manually from the colorless byproduct.

Crystal Structures. Figure 1 shows the molecular structures of **1**−**3**, which are all neutral and centrosymmetric.

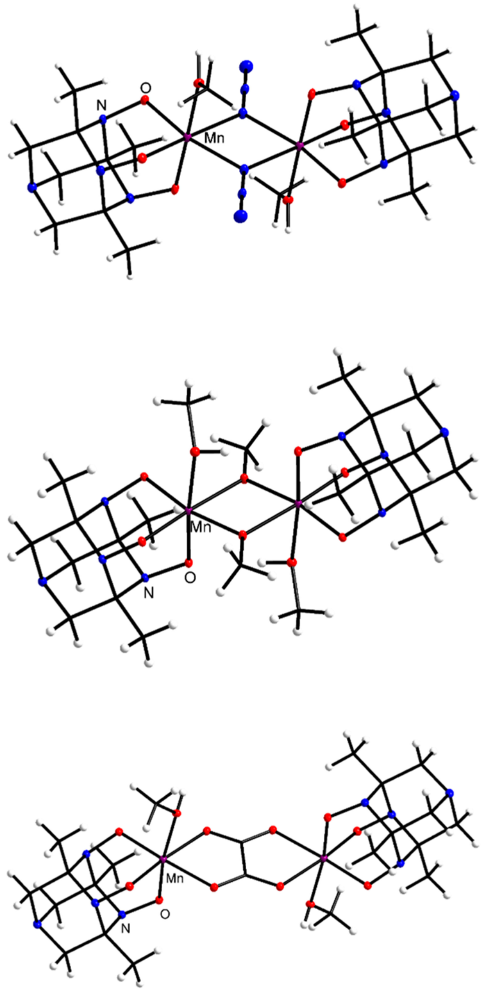

Figure 1. Molecular structures of **1** (top), **2** (center), and **3** (bottom) Thermal ellipsoids of non-C,H atoms are plotted at 20% probability level.

The assignment of +4 formal oxidation state for the manganese ions is supported by the charge balance and bond length analysis.

1 and **3** are methanol solvates, whereas **2** does not contain any molecules of solvation. Table S1 shows selected X-ray data for **1**−**3**. In each complex molecule, two $Mn(L')(CH_3OH)$ units are present which are linked by various bridging ligands: double azide (**1**), double methoxido (**2**), and oxalate (**3**). Each such unit comprises an Mn^{IV} ion with a tridentate *O*,*O*,*O*-coordinated 1,4,6,10-tetraazaadamantane terminal ligand and one terminal methanol ligand. Selected parameters of these bridges are collected in Table S2.

The apical N atom of the terminal trihydroxo-trimethyl-tetraazaadamantane ligand remains uninvolved in coordination to the metal ions regardless of the applied reagents ratio. The free ligand is only known as salt of tartaric acid protonated on the apical N.[17] In the case of the free ligand the oxygen atoms are in axial orientation twice and in equatorial orientation once, whereas in the complexes only axial orientation is observed. The N−O bond lengths are significantly shorter than those in the free ligand, 1.370(3)−1.3881(19) Å in **1**−**3** versus 1.437(3)−1.355(4) Å in the free ligand. The C−N bond lengths are unaffected by the coordination to Mn through O atoms, and complete axial arrangement is observed.

The $Mn(N_3)_2Mn$ diamond-like arrangement is typical of Mn^{III} complexes[44,45] and unprecedented in Mn^{IV} chemistry. An analogous motif with double methoxo bridges in **2** is well-known among Mn^{II} and Mn^{III} compounds. A thorough study on magnetostructural correlations in bis-μ-alkoxo Mn^{III} dimers was reported by Rajaraman and Jones et al.[46] Somewhat less abundant μ-oxalate dimers of Mn^{III} and Mn^{II} have been reported.[47,48]

Hydrogen bonds O−H···N are present in **1** and **3** (Table S3), contrary to **2**. Thus in **1**, **2**, and **3**, undulated hydrogen-bonded layers parallel to (011), overlapping columns parallel to [100] and columns along [100] are formed, respectively (Figure 2).

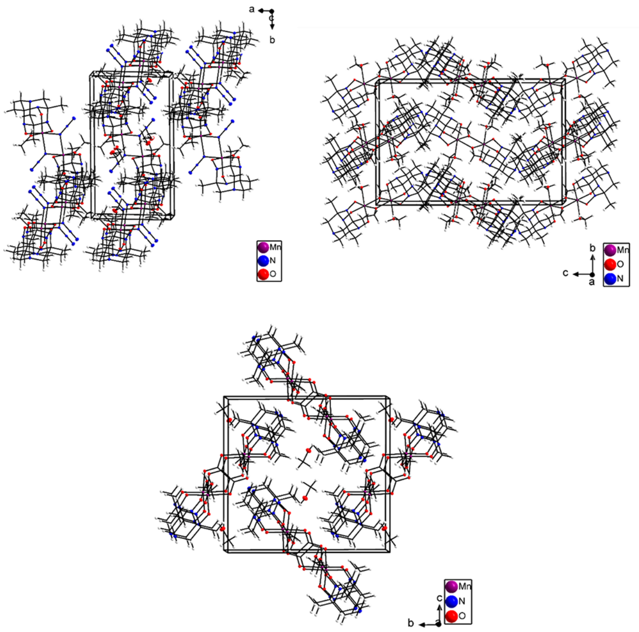

Figure 2. Packing of the complex molecules in **1** (top), **2** (center), and **3** (bottom.).

Magnetic Properties. Magnetic susceptibilities of **1**−**3** were measured from 1.8 to 300 K in applied fields of 500 and 1000 G. The χT versus T plots for **1**−**3**, obtained in a field of 1000 G, are shown in Figure 3. The χT products at 295 K are 4.04 $cm^3\ mol^{-1}$ K, 3.28 $cm^3\ mol^{-1}$ K, and 4.36 $cm^3\ mol^{-1}$ K, for **1**, **2**, and **3**, respectively. The theoretical value expected for two spin-only, $S = 3/2$ Mn^{IV} ions is 3.75 $cm^3\ mol^{-1}$ K. At room temperature, the experimental χT values of **1** and **3** are somewhat higher than the spin-only value which can be explained by considering the contribution of temperature-independent paramagnetism (TIP). The χT value of **2** is significantly lower than the spin-only value which demonstrates a stronger antiferromagnetic coupling of the two Mn^{IV} ions. Decreasing the temperature leads to an initial slight decrease of

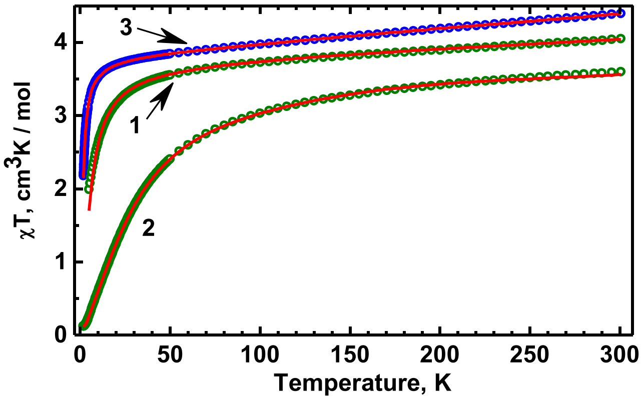

Figure 3. Plot of the $\chi_{\text{mol}}T$ product for complexes **1**, **2**, and **3**. Circles are the experimental points and the continuous lines were calculated using (1) for **1** and **2** and (10) for **3**. Parameters: **1**: $J = -0.80(1)$ cm^{-1}, $g = 1.97(1)$, TIP = 690(10) × 10^{-6} cm^3 mol^{-1}. **2**: $J = -5.00(1)$ cm^{-1}, $g = 1.957(1)$, $a = 0.031$, TIP = 390(10) × 10^{-6} cm^3 mol^{-1}. **3**: $g = 2.01(1)$, $J = -0.21(2)$ cm^{-1}, $D_{\text{Mn}} = -0.85$ cm^{-1} (from EPR, fixed), and TIP of 1000(10) × 10^{-6} cm^3 mol^{-1}.

χT of **1** and **3** followed by a more dramatic drop below 22 and 15 K, respectively, indicating a weak antiferromagnetic coupling of the Mn$^{\text{IV}}$ ions.

For **2** the decrease of χT is more accentuated than those observed for **1** and **3** demonstrating the presence for **2** of a stronger antiferromagnetic coupling.

The exchange coupling constant of **2** was determined using the Heisenberg−Dirac−van Vleck Hamiltonian. We used the $\hat{\mathbf{H}} = -2J\hat{\mathbf{S}}_1\cdot\hat{\mathbf{S}}_2$ formalism which leads to a formula of the magnetic susceptibility (per a dimer), χ_{dim}, described by eq 1a:

$$X_{\text{dim}} = \frac{N\mu_B^2 g^2}{3k_BT}\cdot\frac{6e^{2x} + 30e^{6x} + 84e^{12x}}{1 + 3e^{2x} + 5e^{6x} + 7e^{12x}} \tag{1a}$$

where $x = J/k_BT$. The susceptibility of a monomeric impurity with $S = 3/2$ is given by

$$X_{\text{mono}}\frac{N\mu_B^2 g^2}{3k_BT}\cdot\frac{15}{4} \tag{1b}$$

The total susceptibility can be expressed as

$$\chi = (1 - a)\chi_{\text{dim}} + 2a\chi_{\text{mon}} + 2TIP \tag{1c}$$

where the TIP term of 1c is the temperature-independent paramagnetism contribution of one Mn^{4+} ion.

Least-square fitting of the χ versus T curve for **2** yielded $J = -5.00(1)$ cm^{-1}, $g = 1.957(1)$, $a = 0.031$, and TIP = 390(10) × 10^{-6} cm^3 mol^{-1}. Fitting the magnetic susceptibility of **1** using eq 1c did not yield a high-quality fit as that obtained for **2**. At lower temperatures, the experimental magnetic susceptibility was too high, which could only be simulated assuming an unrealistically large paramagnetic contamination with a monomeric d^3 species. Considering the weak interactions with neighboring molecules (in a form of the zJ parameter) did not improve the fit and using a more sophisticated treatment (taking the zero-field splitting into account, see below) did not help. Analysis of the EPR spectra suggested that **1** is contaminated by Mn$^{\text{III}}$. Nevertheless, since the J parameter strongly affects the curved part of the χT vs T dependence, this analysis still led to an approximate exchange integral value of ca. −0.81(5) cm^{-1}. At higher temperatures, the χT data also indicate presence of a large temperature-independent term of ~700 × 10^{-6} cm^3 mol^{-1} per Mn^{4+} ion. Complex **3** exhibits a very small exchange interaction. Determination of the small J value in this case required a more involved treatment taking into account the zero-field splitting on the Mn^{4+} ions (see below) yielding $g = 2.01(2)$, $J = -0.21(2)$ cm^{-1}, $D = -0.85$ cm^{-1} (value from EPR, fixed), and TIP of 1033 × 10^{-6} cm^3 mol^{-1} per Mn^{4+} ion. The three compounds are differentiated by the strength of the antiferromagnetic coupling and the value of their temperature-independent parameters. The TIP magnitudes obtained here are unexpectedly large. However, such values are not unprecedented and have been observed for other d^3−d^3 dimers including the Mn(IV)[15] and Cr(III) systems.[49a]

HF-EPR Studies, General Comments. The exchange interaction in a d^3−d^3 dimer gives rise to coupled-spin states with S = 0, 1, 2, and 3. The dominant feature of the high-field EPR spectra of **2** is a pattern characteristic of a triplet (S = 1) spectrum, which include a strong "half-field" transition, also called a "forbidden" or "$\Delta M_S = 2$" transition (Figures 4 and 5).

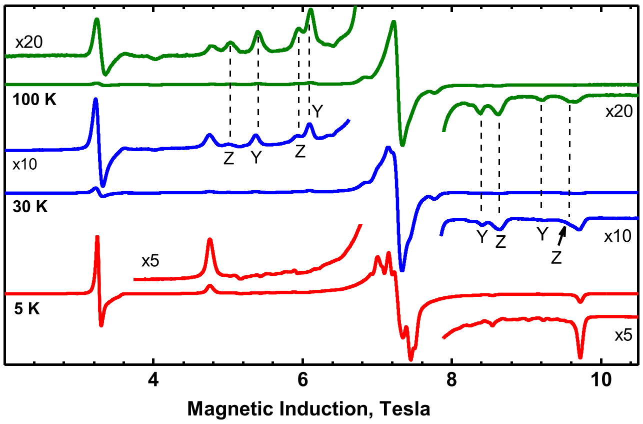

Figure 4. High-field EPR spectra of **2** recorded with the microwave frequency 203.2 GHz at 5 K, 30 and 100 K. The weak wings of the spectra are magnified as indicated. The S = 3 state spectrum is not seen at 5 K. Symbols "y" and "z" indicate the molecular orientations at which the transitions within the S = 3 state occur. See also Figure 5.

Complex **2** exhibits the strongest exchange interaction. Its high-field EPR spectra associated with the S = 1 and 3 spin manifolds could be simulated independently using the giant spin approach (Figure 5) over a wide range of microwave frequencies. The use of the giant spin approximation is not unprecedented for systems such as **1**−**3** and has been successfully used to analyze the S = 3 spectrum of a ferromagnetic Mn(IV) dimer.[14] The spectra recorded for complex **1** also seem to display triplet state features; however, they could not be simulated using the giant spin approach. In this case, the position of the strong, half-field transition could not be reconciled with the positions of the "allowed" (ΔM_S = 1) transitions, particularly at higher frequencies, ~300−420 GHz. For complex **3**, the exchange interactions are so weak that its EPR spectra appear to be very similar to those of a d^3 monomer. However, they could not be satisfactorily simulated using only an S = 3/2 mononuclear site.

Interpretation of the EPR Spectra. The general spin Hamiltonian appropriate for our binuclear systems is

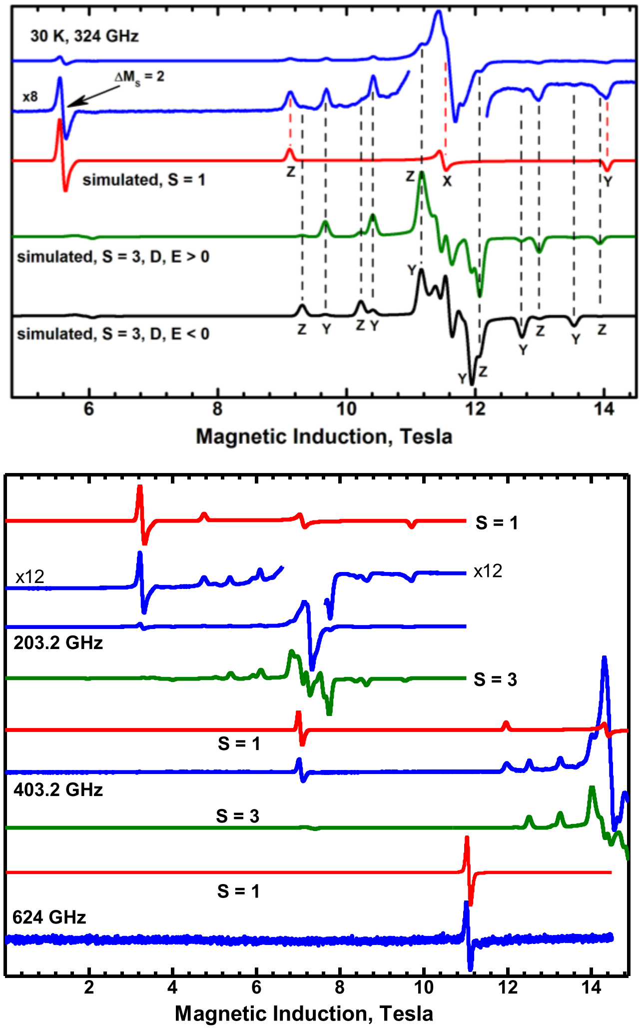

Figure 5. Blue: EPR spectra of **2** recorded at 30 K with the microwave frequency 324.0 GHz (top) and with 203.2, 403.2, and 624.0 GHz (bottom). Different magnetic field range for the two images. Red and green traces show spectra simulated for the spin state $S = 1$ and 3, respectively with parameters from Table 1. The molecular orientations (x, y, and z) at which transitions occur are indicated in the picture at the top. The black trace in the top picture shows simulation for $S = 3$ with negative $D_{S=3}$ and $E_{S=3}$. It is seen that negative ZFS parameters produce an incorrect intensity pattern.

$$\hat{\mathbf{H}} = -2J\hat{\mathbf{S}}_1\hat{\mathbf{S}}_2 + \mu_B\mathbf{B}\{\boldsymbol{g}_1\}\hat{\mathbf{S}}_1 + \hat{\mathbf{S}}_1\{\boldsymbol{D}_1\}\hat{\mathbf{S}}_1 + \mu_B\mathbf{B}\{\boldsymbol{g}_2\}\hat{\mathbf{S}}_2 + \hat{\mathbf{S}}_2\{\boldsymbol{D}_2\}\hat{\mathbf{S}}_2 + \hat{\mathbf{S}}_1\{\boldsymbol{D}_{12}\}\hat{\mathbf{S}}_2 \quad (2)$$

where the individual terms refer to the isotropic exchange, the Zeeman interactions, described by the local single-ion g matrices $\{\boldsymbol{g}_1\}$ and $\{\boldsymbol{g}_2\}$, local zero-field splitting tensors $\{\boldsymbol{D}_1\}$ and $\{\boldsymbol{D}_2\}$, and the interaction tensor $\{\boldsymbol{D}_{12}\}$ which contains the magnetic dipolar and the anisotropic exchange contributions. In our case, dinuclear complexes **1**−**3** have an inversion center; thus, $\{\boldsymbol{D}_1\} = \{\boldsymbol{D}_2\}$. To emphasize that these tensors refer to the local zero-field splitting of the individual Mn ions, we will use the designation $\{\boldsymbol{D}_{\mathrm{Mn}}\}$. Obviously, the g matrices of two ions must be also identical, $\{\boldsymbol{g}_1\} = \{\boldsymbol{g}_2\}$. In the strong exchange limit, i.e., the isotropic exchange interactions are much stronger than the zero-field splitting effects, the Hamiltonian of eq 2 may be conveniently expressed using the total spin operator of the system, $\hat{\mathbf{S}} = \hat{\mathbf{S}}_1 + \hat{\mathbf{S}}_2$. After dropping the first term of eq 2, that is, the isotropic term $-2J\hat{\mathbf{S}}_1\cdot\hat{\mathbf{S}}_2$, which does not affect the EPR resonance positions when $|J|$ is sufficiently large, we can write for each spin state S

$$\hat{\mathbf{H}}_S = \mu_B\mathbf{B}\{\boldsymbol{g}_S\}\hat{\mathbf{S}} + \hat{\mathbf{S}}\{\boldsymbol{D}_S\}\hat{\mathbf{S}} \quad (3)$$

where the $\{\boldsymbol{D}_S\}$ tensors are different in each spin state S.[14,49−52] The transition from Hamiltonian 2 to 3 is accomplished using the spin-coupling coefficients α_S and β_S; see eq 4.[49−52]

$$\begin{aligned} \{\boldsymbol{D}_{\mathbf{S=1}}\} &= 1.7\{\boldsymbol{D}_{\mathbf{12}}\} - 2.4\{\boldsymbol{D}_{\mathbf{Mn}}\} \\ \{\boldsymbol{D}_{\mathbf{S=2}}\} &= 0.5\{\boldsymbol{D}_{\mathbf{12}}\} \\ \{\boldsymbol{D}_{\mathbf{S=3}}\} &= 0.3\{\boldsymbol{D}_{\mathbf{12}}\} + 0.4\{\boldsymbol{D}_{\mathbf{Mn}}\} \end{aligned} \quad (4)$$

In this paper, to interpret the EPR spectra, instead of directly using the spin Hamiltonian of eq 3 we followed the well-established procedure of using that of eq 5:

$$\hat{\mathbf{H}}_S = \mu_B\mathbf{B}\{\boldsymbol{g}_S\}\hat{\mathbf{S}} + D_S\left\{\hat{\mathbf{S}}_z^2 - \frac{1}{3}S(S+1)\right\} + E_S(\hat{\mathbf{S}}_x^2 - \hat{\mathbf{S}}_y^2) \quad (5)$$

Although the exchange interactions in **2** were not strong, we were able to interpret its EPR spectra using the giant spin Hamiltonian 5. Spectra due to the $S = 1$ and 3 states were successfully simulated (Figure 6) using parameters from Table 1. It is seen in Figure 5 that the high-field "y" transitions (at the magnetic fields higher than the central feature) lose intensity when the temperature is lowered from 100 to 30 K, while the low-field transitions remain visible. The opposite is observed for the "z" transitions. This intensity pattern is consistent with a positive $D_{S=3}$. The low-field (4.75 T) and the high-field (9.72 T) features in the $S = 1$ spectrum are the "z" and "y" transitions, respectively, which are at equal distances from the spectrum center because $E_{S=1}$ is very close to $(1/3)D_{S=1}$. The E/D ratios in the triplet and septet states are $E_{S=1}/D_{S=1} = 0.33$ and $E_{S=3}/D_{S=3} = 0.23$. Since the $E_{S=1}/D_{S=1}$ ratio equals 1/3, the sign of $D_{S=1}$ is not important; the same HF EPR $S = 1$ simulation will be produced with either sign. Changing the sign of $D_{S=1}$ in this situation is equivalent to swapping the labels of the Z and Y axes (and swapping the zz and yy components of the $\{\boldsymbol{D}_{S=1}\}$ tensor). The choice of a negative $D_{S=1}$ in Table 1 was convenient for the "alignment" of the $\{\boldsymbol{D}_{S=3}\}$ and $\{\boldsymbol{D}_{S=1}\}$

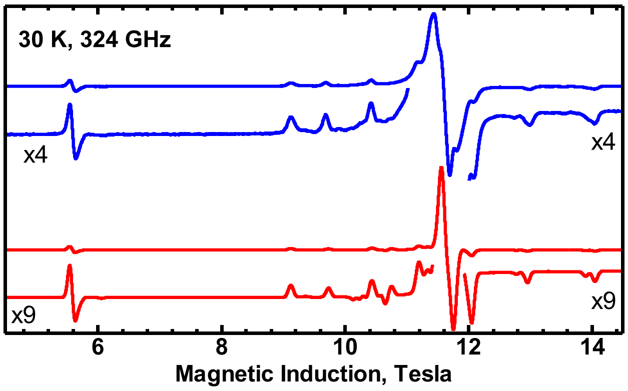

Figure 6. EPR spectrum of **2** (blue trace) and its simulation (red) using the full spin Hamiltonian 7 with $J = -5.00$ cm^{-1}, $D_{\mathrm{Mn}} = 1.00$ cm^{-1}, $E_{\mathrm{Mn}} = 0.281$ cm^{-1}, $D_{12} = 0.069$ cm^{-1}, $E_{12} = -0.052$ cm^{-1}.

Table 1. Giant Spin Hamiltonian Parameters for 2 in the States S = 1 and 3 at 30 K

spin	g_x[a]	g_y	g_z	D, cm^{-1}	E, cm^{-1}	E/D
1	1.993(3)	1.993(3)	1.994(3)	−2.29(1)	−0.76(1)	0.33(1)
3	1.999(1)	1.999(1)	1.993(1)	0.422(2)	0.097(9)	0.23(1)

[a] No x resonances were observed, and g_x was assumed equal to g_y.

tensors in Table 2 (see below). Choosing a positive $D_{S=1}$ would simply result in a different alignment, without changing further results or conclusions. Our g values listed in Table 1 (1.990–1.994) are very similar to those reported for the S = 3 state in another dinuclear Mn(IV) complex,[14] for which $D_{S=3}$ of 0.27 cm^{-1} was determined from high-field EPR. We were not able to clearly identify signals originating from the S = 2 manifold; they must be hidden under the broad central feature, as the zero-field splitting in that state is expected to be small (see below). That central feature is due in part to contaminations or decomposition products, as its intensity increases with sample age, thus further complicating the analysis of the S = 2 contribution to the spectra.

Table 2. Eigenvalues of the Zero-Field Splitting Tensors (cm^{-1}) Obtained for 2

	D_{xx}	D_{yy}	D_{zz}
$\{\boldsymbol{D}_{S=1}\}$[a]	0.003	1.523	−1.526
$\{\boldsymbol{D}_{S=3}\}$[a]	−0.044	−0.237	0.281
$\{\boldsymbol{D}_{12}\}$[b]	−0.075	0.029	0.046
$\{\boldsymbol{D}_{\mathrm{Mn}}\}$[b]	−0.053	−0.614	0.668
$\{\boldsymbol{D}^{\mathrm{dipolar}}\}$[c]	−0.116	0.058	0.058

[a] Experimental. [b] Calculated from eq 10. [c] Calculated from eq 9.

The relations between the scalar D and E parameters of eq 5 and the eigenvalues of $\{\boldsymbol{D}\}$ in eq 3 can be expressed by

$$D = \frac{2D_{zz} - D_{xx} - D_{yy}}{2} \qquad E = \frac{D_{xx} - D_{yy}}{2} \tag{6}$$

while the reciprocal relations are

$$D_{xx} = -D/3 + E$$
$$D_{yy} = -D/3 - E$$
$$D_{zz} = 2D/3 \tag{6a}$$

Note that eqs 6a produce components of a traceless tensor ($D_{xx} + D_{yy} + D_{zz} = 0$), while eqs 6 does not require a traceless tensor.

The spin Hamiltonian 2 can also be rewritten using the scalar zero-field splitting parameters:

$$\begin{aligned}\hat{\mathbf{H}} = {} & -2J\hat{\mathbf{S}}_1\hat{\mathbf{S}}_2 + \mu_{\mathrm{B}}\mathbf{B}\{\boldsymbol{g}_1\}\hat{\mathbf{S}}_1 + \mu_{\mathrm{B}}\mathbf{B}\{\boldsymbol{g}_2\}\hat{\mathbf{S}}_2 \\ & + D_{\mathrm{Mn}}\left\{\hat{\mathbf{S}}_{z1}^2 - \frac{1}{3}S(S+1)\right\} + E_{\mathrm{Mn}}(\hat{\mathbf{S}}_{x1}^2 - \hat{\mathbf{S}}_{y1}^2) \\ & + D_{\mathrm{Mn}}\left\{\hat{\mathbf{S}}_{z2}^2 - \frac{1}{3}S(S+1)\right\} + E_{\mathrm{Mn}}(\hat{\mathbf{S}}_{x2}^2 - \hat{\mathbf{S}}_{y2}^2) \\ & + D_{12}\left\{\hat{\mathbf{S}}_{z1}\hat{\mathbf{S}}_{z2} - \frac{1}{3}\hat{\mathbf{S}}_1\hat{\mathbf{S}}_2\right\} + E_{12}(\hat{\mathbf{S}}_{x1}\hat{\mathbf{S}}_{x2} - \hat{\mathbf{S}}_{y1}\hat{\mathbf{S}}_{y2})\end{aligned} \tag{7}$$

We note that the coefficients in eqs 4 also relate the scalar parameters D_S to D_{12}, D_{Mn} and E_S to E_{12}, E_{Mn} in spin Hamiltonian 5.[50a] Both the dipole–dipole and anisotropic exchange interactions contribute to the $\{\boldsymbol{D}_{12}\}$ tensor; see eq 8:

$$\{\boldsymbol{D}_{12}\} = \{\boldsymbol{D}^{\mathrm{dipolar}}\} + \{\boldsymbol{D}^{\mathrm{exchange}}\} \tag{8}$$

The dipolar part can be calculated from the formula[53] for which centrosymmetric dimers with practically isotropic g tensors such as those of **1**–**3**, take very simple forms:[49a,54–56]

$$D_{xx}^{\mathrm{dipolar}} = \frac{-2g_x^2\mu_{\mathrm{B}}^2}{R^3}$$
$$D_{yy}^{\mathrm{dipolar}} = \frac{g_y^2\mu_{\mathrm{B}}^2}{R^3}$$
$$D_{zz}^{\mathrm{dipolar}} = \frac{g_z^2\mu_{\mathrm{B}}^2}{R^3} \tag{9}$$

For eqs 9, "x" is assumed to be along the Mn–Mn direction and for the a Mn–Mn distance of 3.1 Å, we obtain $D_{xx}^{\mathrm{dipolar}} = -0.116$ cm^{-1}, $D_{yy}^{\mathrm{dipolar}} = 0.058$ cm^{-1}, and $D_{zz}^{\mathrm{dipolar}}$=0.058 cm^{-1}. The reason for labeling the Mn–Mn direction "x" rather than "z" in formulas (9) is that the largest component of the $\{\boldsymbol{D}_{\mathrm{Mn}}\}$ tensor is expected to be perpendicular to the MnOOMn plane and it is convenient for our discussion to consider this direction as "z". The D^{dipolar} tensor components above are likely to be overestimated, as no electron delocalization is taken into account in eqs 9.[54−56] The zero-field splitting in the S = 2 state of a dimer composed of two S = 3/2 ions depends only on $\{\boldsymbol{D}_{12}\}$, but not on $\{\boldsymbol{D}_{\mathrm{Mn}}\}$ as long as the giant spin model is applicable.[49,50] Since the g tensors are nearly isotropic, indicating no significant spin–orbit coupling effects, no significant contribution of the anisotropic exchange is expected. Therefore, $\{\boldsymbol{D}_{12}\}$ eigenvalues, or alternatively D_{12} and E_{12} are expected to be small, possibly of the same order as the dipolar contributions. Table 2 presents the eigenvalues of $\{\boldsymbol{D}_{S=1}\}$ and $\{\boldsymbol{D}_{S=3}\}$ obtained via eqs 6a. Starting from the known values of $\{D_{S=1}\}$ and $\{\mathrm{D}_{S=3}\}$, we may try to extract the $\{\boldsymbol{D}_{\mathrm{Mn}}\}$ and $\{\boldsymbol{D}_{12}\}$ with the help of eqs 4. There is a problem, however: The orientation of $\{\boldsymbol{D}_{S=3}\}$ versus $\{\boldsymbol{D}_{S=1}\}$ is not available from our experiments. To determine the relative orientations of the D_S tensors, we would need either single-crystal EPR data[49d] or better resolved high-field powder EPR spectra (in particular, with sufficiently resolved S = 2 state resonances).[49a] We are thus forced to assume that the ZFS tensors of S = 1 and 3 manifolds are diagonal in two parallel systems of coordinates, in which the equally named axes may, but do not have to, be parallel to each other, for example, $X_{S=1}$ being parallel to $Z_{S=3}$. This means that before applying eqs 4 we still have to properly "align" the eigenvalues of $\{\boldsymbol{D}_{S=3}\}$ and $\{\boldsymbol{D}_{S=1}\}$. If this "alignment" results in a small $\{\boldsymbol{D}_{12}\}$, which is not guaranteed *a priori*, then our method will be validated. Table 2 shows the diagonal tensor elements of $\{\boldsymbol{D}_{S=3}\}$ and $\{\boldsymbol{D}_{S=1}\}$, which have already been properly "aligned", with $X_{S=3}$ axis parallel to $X_{S=1}$, $Y_{S=3}$ parallel to $Y_{S=1}$, and $Z_{S=3}$ parallel to $Z_{S=1}$. From eqs 4, we have

$$\{\boldsymbol{D}_{12}\} = \frac{\{\boldsymbol{D}_{S=1}\} + 6\{\boldsymbol{D}_{S=3}\}}{3.5}$$

$$\{\boldsymbol{D}_{\mathrm{Mn}}\} = \frac{1.7\{\boldsymbol{D}_{S=3}\} - 0.3\{\boldsymbol{D}_{S=1}\}}{1.4} \tag{10}$$

These operations are performed for the first two rows of Table 2 leading to the $\{\boldsymbol{D}_{12}\}$ and $\{\boldsymbol{D}_{\mathrm{Mn}}\}$ shown in the third and fourth rows of that table. Note that the largest errors in the experimental D and E parameters for S = 1 and 3 are about 10^{-2} cm^{-1} (Table 1); thus, the errors in parameters reported in Table 2 are expected to be of the same order of magnitude. Nevertheless, calculations in Table 2 use 3 digits after the decimal point to demonstrate how the numbers combine. An interested reader may check that no other "alignment" (that is a permutation of the $\{\boldsymbol{D}_{S=3}\}$ elements while leaving those of $\{\boldsymbol{D}_{S=1}\}$ in place) will result in small $\{\boldsymbol{D}_{12}\}$. It is thus seen that it is indeed possible to combine the $\{\boldsymbol{D}_{S=1}\}$ and $\{\boldsymbol{D}_{S=3}\}$ tensors in such a way that a small $\{\boldsymbol{D}_{12}\}$ is obtained. Moreover, the $\{\boldsymbol{D}_{12}\}$ eigenvalues resulting from this calculation, D_{12x} = −0.076 cm^{-1}, D_{12y} = 0.029 cm^{-1}, and D_{12z} = 0.046 cm^{-1}, are close to the dipolar contributions calculated above, i.e, −0.116, 0.058, and 0.058 cm^{-1}, respectively. The large negative eigenvalues of both $\{\boldsymbol{D}_{12}\}$ and $\{\boldsymbol{D}^{\mathrm{dipolar}}\}$ are found along the x-direction, that is, along the intermetallic axis. This argument validates our method and confirms that the anisotropic Mn···Mn interactions are mostly or exclusively of the dipolar character. The $\{\boldsymbol{D}_{\mathrm{Mn}}\}$ and $\{\boldsymbol{D}_{12}\}$ tensors can be converted back to the scalar D and E parameters leading to D_{Mn} = 1.00(1) cm^{-1}, E_{Mn} = 0.28(1) cm^{-1}, ($E_{\mathrm{Mn}}/D_{\mathrm{Mn}}$ = 0.28), D_{12} = 0.069 cm^{-1}, and E_{12}= −0.052 cm^{-1}. Simulations obtained using these parameters and spin Hamiltonian of eq 7 that operates on the entire base of 16 spin functions reproduced reasonably the experimental spectra (Figure 6) and thus validate the simpler giant spin analysis. The likely reason for discrepancies between the experimental and simulated spectrum in Figure 6 is the simplifying assumption of the $\{\boldsymbol{D}_{S=1}\}$ and $\{\boldsymbol{D}_{S=3}\}$ tensors being exactly coaxial, as explained above. It should be mentioned here that both the microscopic and giant spin descriptions of the d^3–d^3 dimers have been found to be imperfect.[49d] The discrepancies are observed mainly in the central part of the spectra, which is affected by decomposition products, as mentioned above. The main result of the EPR experiments are the D_{Mn} and E_{Mn} parameters which are not affected much by the possibly incorrect assumed orientation of $\{\boldsymbol{D}_{\mathrm{Mn}}\}$ versus $\{\boldsymbol{D}_{12}\}$, thanks to the smallness of the latter. An interested reader may note that if the $\{\boldsymbol{D}_{12}\}$ components were assumed zero, D_{Mn} could be estimated from $-D_{S=1}/2.4$ = 0.95 cm^{-1}, or from $D_{S=3}/0.4$ = 1.05 cm^{-1}, both within 5% from the value obtained above.

Energy Levels of the Coupled System in 2. Figure 7 shows that for **2** the energy levels are arranged in easily recognizable multiplets with S = 3, 2, 1, and 0. The mixing of states belonging to different multiplets is weak, and the EPR intermultiplet transition probabilities are low, thus explaining the success of the giant spin approach. A similar problem was solved,[49a] involving a Cr^{3+} dimer where the better-defined spectra afforded a more comprehensive analysis, including the determination of the D and E in the S = 2 state. In that case, the giant spin Hamiltonian was also successfully employed to interpret the HF EPR spectra of complexes with exchange interaction slightly stronger and ZFS substantially smaller than in **2**. According to eqs 4, the D and E parameters in the S = 2 state should be $D_{S=2}$ = 0.034 cm^{-1} and $E_{S=2}$ = −0.025 cm^{-1}. Because of these small $D_{S=2}$ and $E_{S=2}$ values, the resonances associated with the S = 2 state are masked by the broad central feature seen in Figures 4–6. This was confirmed by simulations with either the spin Hamiltonian 5 or 7. X-Band EPR spectra were recorded in a hope to determine the $D_{S=2}$ and $E_{S=2}$ parameters; see Figure S10. Unfortunately, this was not successful as the resolution was not better than in our high-field EPR spectra. It is interesting to note that the EPR resonances within the nominal S = 1 and 3 states in **2** are simulated similarly by using either the microscopic Hamiltonian 7 or the giant spin Hamiltonian 5 with appropriately converted parameters. However, the resonances within the S = 2 state are simulated quite differently if the isotropic exchange is too weak. The splitting calculated with the microscopic Hamiltonian in **2** is much smaller than that resulting from the giant spin model, and no pattern of equally spaced four transitions is found at any frequency, both in HF and X-Band EPR. It has been reported[49d] that it is not possible to fully simulate spectra of Cr(III) dimers using either the giant spin model or the microstate Hamiltonian. This situation was improved by introducing a modified giant spin model with two additional parameters reflecting the mixing of the dimer states |0, 0⟩ with |2, 0⟩ and between states belonging to S = 1 and 3. However, the method was developed for the axial symmetry and would presumably require more additional parameters in our very rhombic case. A comment on the applicability of the giant spin approximation should be made here. It is seen in Figure 7 that the energy levels belonging to different spin states intersect at high magnetic field, but no "anticrossing" effects are seen in Figure 7, which was calculated at the Z orientation. Moreover, no "anticrossing" is seen at other canonical orientations, X and Y, and even at the orientations between the axes. (Figures S6, S7). Thus, with the relations between the parameters as in **2**, J = −5.0 cm^{-1}, D_{Mn} = 1.00 cm^{-1}, and E_{Mn} = 0.28 cm^{-1} ($E_{\mathrm{Mn}}/D_{\mathrm{Mn}}$ = 0.28), the levels belonging to different S states do not interact, even when they have been brought close to each other by the Zeeman interaction. Because the levels do not mix, the intermultiplet transition probabilities are zero (Table S5). The spectra due to different spin states are thus independent and the giant spin model works perfectly, at least for the S = 1 and 3 states, as seen in Figures 4 and 5. A

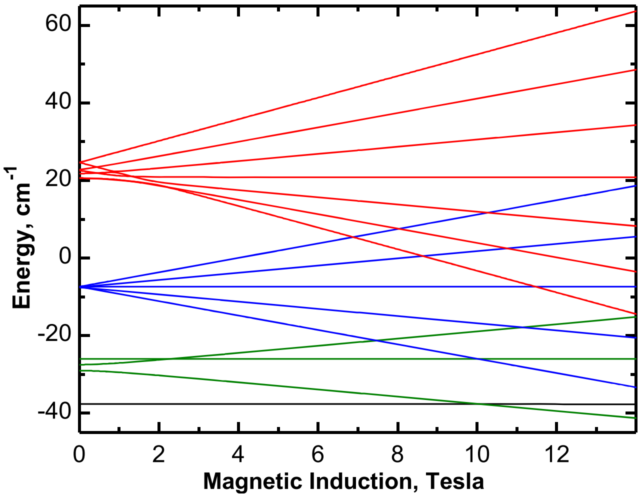

Figure 7. Energy levels of **2** calculated using spin Hamiltonian 7 at the Z orientation of the zero-field splitting tensor $\{\boldsymbol{D}_{\mathrm{Mn}}\}$. The levels belonging to spin states with S = 3, 2, 1, and 0 are drawn as red, blue, green, and black lines, respectively.

weakly ferromagnetic ($J = 11$ cm^{-1}) dimeric Mn(IV) complex of 1,4,7-trimethyl-1,4,7-triazacyclononane was studied by HF EPR.[14] The giant spin method was employed to interpret the $S = 3$ spectra at 285 GHz and positive $D_{S=3}$ of 0.27 cm^{-1} and $E_{S=3} = 0.05$ cm^{-1} were reported, leading to $D_{Mn} = 0.68$ cm^{-1} which is not dramatically different from our results. No signals from the excited $S = 1$ and 2 states could be observed, presumably due to fast relaxation effects at higher temperatures. Interestingly, inability to observe spectra of thermally excited states in ferromagnetic systems may be a more widespread problem. In a series of ferromagnetic trinuclear Cu^{2+} systems only the ground quartet state was observed in EPR.[56]

Energy Levels of the Coupled System in 1 and 3. For the two other complexes, **1** and **3**, the situation is quite different. The exchange interaction is much weaker in azido-bridged complex **1** (−0.85 cm^{-1}), and weaker yet in the oxalate-bridged **3** (−0.21 cm^{-1}). The energy levels calculated for **1** and **3** are shown in Figures 8 and S9, respectively. Our attempts of applying the giant spin method to analyze the HF EPR spectra of **1** and **3** were unsuccessful. This failure can be traced to the zero-field splitting being larger in these systems than the exchange interaction which leads to a strong mixing of the spin multiplets (Figures 8 and S9, Tables S5−S7). In such situations, transitions between different states of the total spin (like between $S = 1$ and 3) are not strictly forbidden and affect the spectra. A very large number of transitions may be present, particularly in a powder spectrum and simulations of a quality similar to those of **2**, proved to be impossible. For **2**, the resonances observed at different frequencies can be easily grouped into "branches" (Figures S4 and S5). In contrast, particularly in **1** (Figure S8), resonances appear and disappear even when frequency is changed over a small range. Analysis of the HFEPR spectra recorded for **1** is made more difficult by the fact that **1** appears to contain Mn^{3+} contamination, as near zero-field transitions are observed at frequencies above 600 GHz. These transitions must occur between states split in zero magnetic field by energy of the order of 20 cm^{-1}. No such splitting is possible in **1** with $|J| < 1$ cm^{-1} and D_{Mn} of the order of 1 cm^{-1}, but it is possible in Mn^{3+} with $|D|$ close to 5 cm^{-1}.[57]

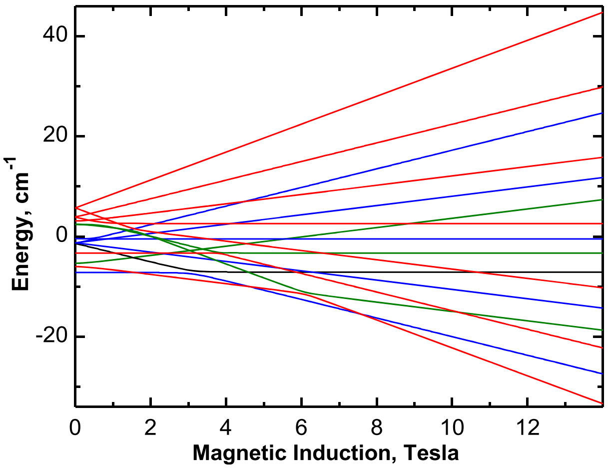

Figure 8. Energy levels of **1** calculated with the spin Hamiltonian 7 at the Z orientation of the zero-field splitting tensor $\{\boldsymbol{D}_{Mn}\}$. The levels which at high magnetic field belong to spin states with $S = 3$, 2, 1, and 0 are drawn as red, blue, green and black lines, respectively. Note that due to the spin state mixing there is no simple correspondence between the high- and low-field states, opposite to the situation in Figure 7. See also Figure S9 for **3**.

Since we were unable to reconcile the magnetic data of **1** with its EPR spectra, these data are presented in the Supporting Information with a detailed explanation of the problems encountered. Nevertheless, it was possible to estimate $D_{S=1}$ of −2.10(1) cm^{-1}, and $D_{Mn} = +0.79(1)$ cm^{-1} (Figure S8). When compared to other cases the D_{Mn} parameters found in this paper are moderate, close to 1 cm^{-1}. It has been shown by theoretical calculations recently that the D magnitude in monomeric Mn^{IV} is dominated by the spin-flip transitions within the approximate t_{2g} levels and it tends to be positive.[58] Negative D_{Mn} observed in some compounds were attributed to the presence of empty ligand orbitals between the (mainly) metal t_{2g} and e_g orbitals.[58] In this paper we found negative D_{Mn} only for **3**.

In the case of the oxalate complex, the exchange interaction is very small, and a question may arise whether its spectra (Figure 9) can be simulated assuming an $S = 3/2$ monomer. Such simulations were indeed somewhat successful and allowed us to estimate D_{Mn} and E_{Mn}. However, the $S = 3/2$ simulation does not reproduce properly the weak half-field signal seen in these spectra.

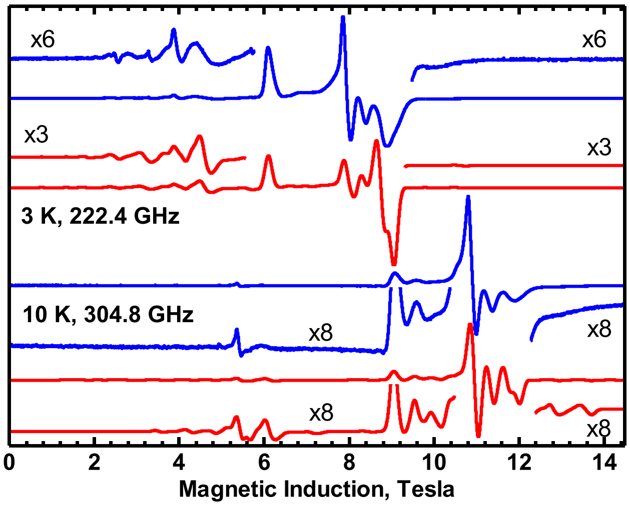

Figure 9. Blue: EPR spectra of **3** recorded at 3 K with microwave frequencies as indicated. The low-intensity wings of the spectra were magnified as indicated. The red traces were simulated using the full spin Hamiltonian 7 with $g_x = g_y = g_z = 1.993$, $D_{Mn} = -0.85$ cm^{-1}, $E_{Mn} = -0.03$ cm^{-1}, $J = -0.21$ cm^{-1}, $D_{12} = -0.032$ cm^{-1}, and $E_{12} = 0$.

For the oxalate complex, the long Mn−Mn distance of 5.44 Å results in a dipolar contribution (estimated using eqs 9 and 6) to D_{12} (eq 7) of −0.032 cm^{-1}, assuming the Z axis along the Mn−Mn direction. The zero-field splitting is thus dominated by D_{Mn} even more than in **2**. With D_{12} fixed at that value, D_{Mn} and E_{Mn} were adjusted to obtain a reasonable simulation of the experimental spectra. The results are $g_x = g_y = g_z = 1.993(1)$, $D_{Mn} = -0.85(1)$ cm^{-1}, $E_{Mn} = -0.03(1)$ cm^{-1}, $J = -0.21(2)$ cm^{-1} (from the magnetic data), $D_{12} = -0.032$ cm^{-1} (calculated), and $E_{12} = 0$ (assumed). It should be understood that the spectra are envelopes of a very large number of transitions in the system of 16 $|S, M_S\rangle$ levels (Figure S9). For example, 17 transitions of substantial probability are found both at the X and at the Z orientations, some of them occurring between states differing in $\langle S^2\rangle$, thus being intermultiplet transitions (see Tables S5−S7). Just 3 $\Delta M_S = 1$ and 2 $\Delta M_S = 2$ transitions are expected for an $S = 3/2$ monomer at any molecular orientation.

Since the zero-field splitting in **3** has now been determined, we may go back to the analysis of its magnetic properties. Compounds **1** and **3** exhibit large magnetic susceptibility at the lowest temperatures. Under these conditions predicting the magnetic susceptibilities using eqs 1 becomes problematic, as the splitting of energy levels caused by the Zeeman and zero-field splitting interactions are comparable to kT at low temperatures. To take these splittings into account, the magnetic susceptibility of a dimer may be calculated from the fundamental formula

$$\chi_{\text{dim}} = -\frac{N\sum_i \frac{\partial E_i}{\partial B}\, e^{-E_i/kT}}{B\sum_i e^{-E_i/kT}} + 2\text{TIP} \tag{11}$$

where the summation runs over all 16 states in the system. The energies E_i were determined by diagonalizing the matrix of the spin Hamiltonian described by eq 7. The $\partial E_i/\partial B$ derivatives were calculated numerically, by evaluating energies E_i 5 G below and 5 G above the magnetic field of the SQUID instrument (1000 G). Equation 11 gives the magnetic susceptibility $\chi(\Theta, \Phi)$ at an orientation of a molecule versus the magnetic field and needs still to be averaged over all orientations, which is accomplished by numerical integration of $\chi(\Theta, \Phi) \sin\Theta\, d\Theta\, d\Phi$, in manner similar to that of powder EPR spectra are calculated. For the three cases presented in this paper, the results obtained using eqs 1 or the method described above are very similar. The strongest effect is observed in weakly interacting complex **3**. When using eq 11 and fixing D_{Mn}, E_{Mn}, and D_{12} as found from EPR above, the fitting results in $g = 2.01(1)$, $J = -0.21(2)$ cm^{-1} and TIP of $1033(10) \times 10^{-6}$ cm^3 mol^{-1}. The g value obtained in this way, which is larger by 0.8% than found from EPR (and impossible for a d^3 ion for which g must be smaller than 2.0023) may be caused by a partial loss of the solvent (CH_3OH) for the sample used for the magnetic measurements which leads to overestimation errors when converting the gram-susceptibility to molar susceptibility. Figure 10 shows the χT product of **3** as a function of temperature, calculated with eq 11. Simulations that best resemble the experiment are obtained when using the parameters given above. It is also seen that neglecting zero-field splitting affects the calculated χT values only slightly, while the isotropic exchange effect is strong, despite D_{Mn} being much larger than J.

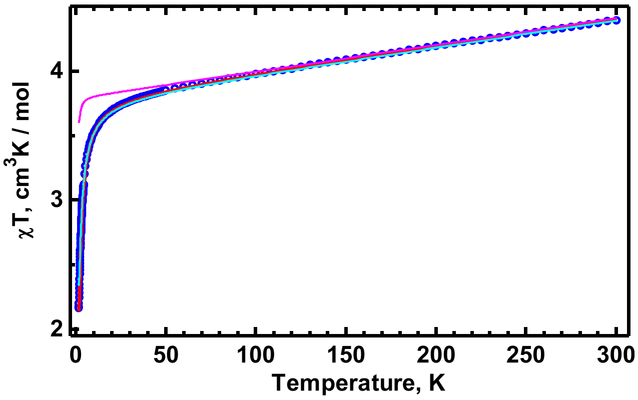

Figure 10. Product χT of **3** as a function of temperature. Blue circles: experimental. Red: calculated with $g = 2.01$, $J = -0.21$ cm^{-1}, TIP = 1033×10^{-6} cm^3 mol^{-1}, $D_{\text{Mn}} = -0.85$ cm^{-1}, and $E_{\text{Mn}} = -0.03$ cm^{-1}. Magenta: calculated as two noninteracting monomers, $g = 2.01$, $J = 0$, TIP = 1033×10^{-6} cm^3 mol^{-1}, $D_{\text{Mn}} = -0.85$ cm^{-1}, and $E_{\text{Mn}} = -0.03$ cm^{-1}. Cyan: Dimer with no zero-field splitting, $g = 2.01$, $J = -0.21$ cm^{-1}, TIP = 1033×10^{-6} cm^3 mol^{-1}, $D_{\text{Mn}} = 0$ cm^{-1}, and $E_{\text{Mn}} = 0$.

Theoretical Analysis of 1−3. *Electronic Structure of the 4,6,10-Trihydroxo-3,5,7-trimethyl-1,4,6,10-tetraazaadamantane Ligand.* One of the most intriguing features of the adamantane-like ligand supporting **1−3** is that it incorporates three NO moieties. Typically, such molecules either function as spin traps or they exhibit a paramagnetic ground state.[59,60] The +4 formal oxidation state of the metal ions implies a −3 charge for each of the two L′ ligands. Owing to the higher electronegativities of the N and O atoms when compared to the C atoms, we expect the ligand charges to be mainly accommodated by the NO groups and to lead to the formation of three anionic NO$^-$ moieties. However, our theoretical investigation of **1−3**, *vide infra*, suggested that in the presence of an oxidized metal ion such Mn(IV) the ligand is redox noninnocent. To evaluate this fact, we have explored the electronic structure of the free ligand using computational methods (see section 10 of the Supporting Information) and its redox reactivity using CV and X-band EPR. These investigations revealed that when the free ligand is deprotonated it is easily oxidized to yield an EPR-active radical anion. Thus, cyclic voltammetry of the ligand revealed the presence of an irreversible oxidation wave at +0.15 V vs Fc^0/Fc$^+$; see Figures 11 and S13. This observation was further corroborated by X-band EPR spectroscopy which showed that basic solutions of the free ligand are readily oxidized by molecular oxygen; see Figure S14. In this respect, the formation and the lifetime of the ligand-derived EPR-active species is similar to that of the *o*-benzosemiquinone radical anion obtained from catechol.[61] Moreover, the ligand can be also oxidized by mild oxidants such as ferricyanide. Regardless of the oxidant used, the resulting EPR active species exhibits a hyperfine splitting pattern typical of NO-based radicals; see Figure 11.[62]

Charge and Spin Distributions of 1−3. To examine the electronic structures of **1−3**, we have performed a series of DFT calculations using the B3LYP, BP86, and TPSSH functionals in combination with the 6-311G, 6-311G*, and 6-311+G** basis sets. The B3LYP/6-311G functional/basis set combination has been used extensively in the investigation of transition metal complexes. Our choice of functionals allows us to compare results obtained using hybrid functionals that have been shown to yield reliable predictions of spectroscopic parameters, B3LYP and TPPSh, with those obtained using a nonhybrid functional that has been used to evaluate the ZFS parameters of Mn(IV) sites, BP86.[58] While BP86 tends to emphasize over-delocalization, a behavior typical of GGA functionals, the Hartree−Fock exchange incorporated in the hybrid B3LYP functional leads to the increased stabilization of high-spin states which in our case, favors configurations for which the ligands are redox noninnocent.[63] Previous investigations of Mn(III) and Mn(IV) complexes found that B3LYP functional yielded the best prediction of ZFS parameters.[64] Concomitantly, it has been also suggested that using BP86 might provide the most cost-effective method to obtain relatively accurate theoretical values.[64] Among these three functionals, TPPSh performed better when used to predict the exchange coupling constants of [Mn(III)Mn(IV)] mixed

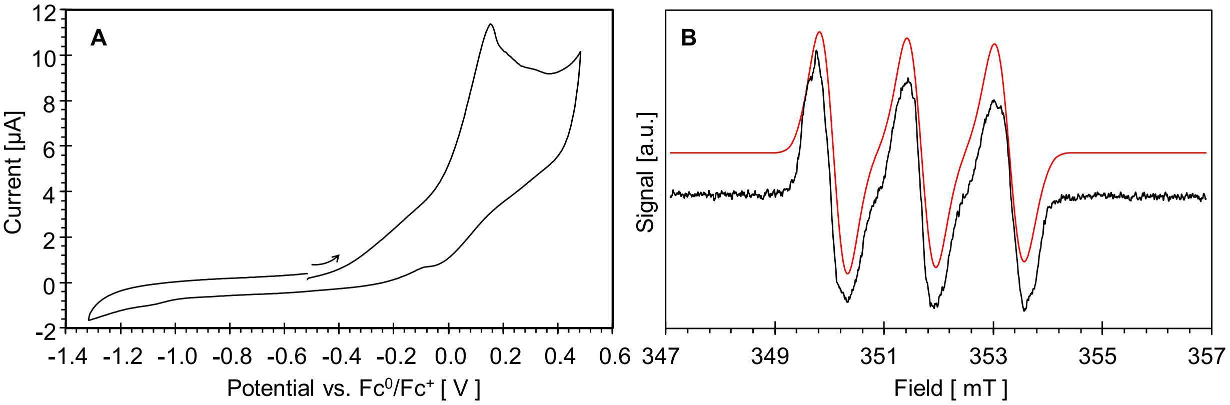

Figure 11. (A) Cyclic voltammogram of the free ligand. This trace was obtained for a NaOH saturated solution of 2 mM free ligand using as supporting electrolyte 0.1 M NBu_4PF_6, in DMSO, at a scan rate of 100 mV/s. (B) X-band EPR spectrum obtained for a 0.1 M NaOH, 0.1 M $K_3[Fe(CN)_6]$, and 50 mM free ligand water solution. The spectrum shown here was recorded within 1 min after mixing the ligand and basic ferricyanide solutions, using a Bruker AquaX cell, at room temperature. Instrumental conditions were 20 mW microwave power, 0.5 G modulation amplitude, and 9.873 GHz microwave frequency. The solid red line is a simulation obtained for a system consisting of a $S = 1/2$ and $I = 1$ spins with $g_{iso} = 2.006$, $\sigma(g_{iso}) = 2 \times 10^{-3}$, $A_{iso} = 45.3$ MHz, $\sigma(A_{iso}) = 2 \times 10^{-3}$ MHz, and a line width of 0.8 G.

Table 3. Theoretical Exchange Coupling Constants, *J* [cm^{-1}], Obtained Using the BP86, B3LYP, and TPSSH Functionals in Combination with the 6-311G, 6-311G*, 6-311+G, and TZVP Basis Sets**

method		struct.	complex/*J* [cm^{-1}]		
			1	**2**	**3**
B3LYP	6-311G	X-ray	2.16	−2.29	1.03
	6-311G	optimized	−1.38	1.31	0.22
	6-311G*	optimized	−1.70	−1.14	0.29
	6-311+G**	optimized	−0.02	−1.61	0.00
	TZVP(Mn)[a]	X-ray	0.4	−3.2	1.4
BP86	6-311G	X-ray	−4.41	−28.31	−1.34
	6-311G	optimized	−9.60	−21.82	−2.04
	6-311G*	optimized	6.49	−19.77	−1.74
	6-311+G**	optimized	6.28	−19.66	−1.74
TPSSH	6-311G	X-ray	1.07	−5.67	0.97
	6-311G	optimized	8.44	−3.77	0.09
	6-311G*	optimized	−0.51	−4.49	0.47
	6-311+G**	optimized	11.62	−3.58	0.43
experimental			−0.80(1)	−5.00(1)	−0.21(1)

[a] The TZVPP basis set was used only for Mn and all coordinated atoms, while for all other atoms SVP[30−34] was employed.

valence complexes.[65,66] However, in our case, not only do these functionals predict ground state configurations that exhibit divergent metal ion and ligand oxidation states but also the ZFS parameter values depend on whether theoretical or experimental structures are used, *vide infra*.

The HF EPR spectra of **1**−**3** were successfully interpreted considering two weakly interacting quartet spin sites. Consequently, we have performed a series of calculations starting from initial guesses for which the [L′Mn] moieties were monocationic and had a $S = 3/2$ ground spin state. Except for the oxalate which is dianionic, the individual bridging ligands are monoanionic. A guess which assumes redox-innocent ligands concomitantly implies the presence of a genuine Mn(IV) ions with a d^3 electronic configuration. However, inspection of Table S11 shows that for a mononuclear [L′Mn] fragment a quartet ground spin state can be obtained not only for a formal Mn(IV) but also for Mn ions that have +3 and +2 oxidation states. The increase in the electron count of the metal sites from d^3 to d^5 is facilitated by the ligand-to-metal transfer of one or more electrons, which yields paramagnetic ligands. Our analysis of the $\langle \hat{S}^2 \rangle$ expectation value, included in section 11 of the Supporting Information, suggests that while the BP86 and TPPSh-predicted electronic configurations are consistent with a +4 formal oxidation state of the Mn sites those predicted by B3LYP are indicative for the presence of Mn(III) ions that have a quintet spin state antiferromagnetically coupled to the $S = 1/2$ spin of tetraazaamantane ligands. These conclusions are further corroborated by the Mulliken atomic spin densities predicted for the Mn ions which are 0.6−0.9 spins higher when using B3LYP than those obtained for the BP86 and TPSSh functionals, see Table S12 and Figure S15. Interestingly, inspection of Tables S12−S15 shows that the predicted charges are far less sensitive on the choice of functional and that as expected the natural populations of the valence shells

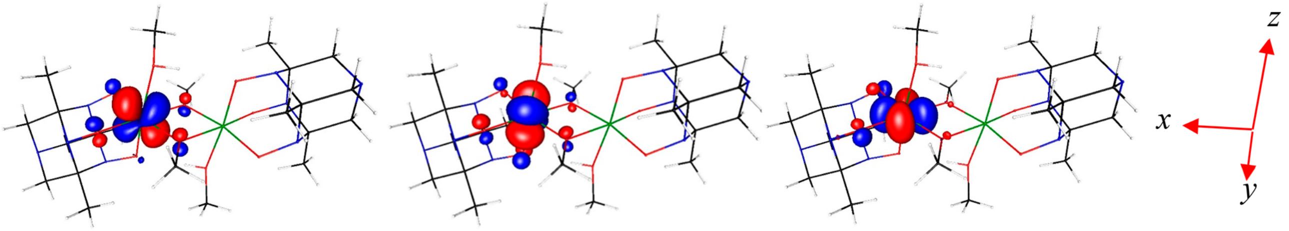

Figure 12. Magnetic orbitals *xz*, *yz*, and *xy* (from left to right) of one of the Mn ions in **2**. In each case, an orbital of identical shape is located on another Mn ion. The system of coordinates is also shown. All three plots are in the same orientation, and the axes of two Mn ions are parallel.

Table 4. Theoretical Zero-Field Splitting Parameters of Quartet Ground States Predicted for the Local Metal Sites of Complexes 1−3[a]

#	method	D	E/D	D_{SS}	*contribution to* $\mathbf{D}_{SOC}$			
					$\alpha\to\alpha$	$\beta\to\beta$	$\alpha\to\beta$	$\beta\to\alpha$
1	***experimental***	***0.79***	***0.15***	*n.a.*				
	CASSCF(3,5)	−0.324	0.058	−0.015	−0.199		−0.125	n.a.
	NEVPT2(3,5)	−0.421	0.141	−0.015	−0.050		−0.371	n.a.
	CASSCF(7,7)	−3.028	0.052	−0.040	−0.961		−2.067	n.a.
	NEVPT2(7,7)	−2.826	0.063	−0.040	−0.575		−2.251	n.a.
	B3LYP/6-311G	*0.618*	*0.279*	*0.111*	*0.097*	*0.111*	*0.592*	*−0.294*
		$-1.109^{b,c}$	0.212^{b}	−0.020	−0.212	−0.077	−0.420	−0.378
	BP86/6-311G	0.543	0.185	0.143	0.043	0.155	0.222	−0.020
		0.543^{b}	0.083^{b}	0.114	0.055	0.128	0.264	−0.019
	TPSSH/6-311G	1.890	0.045	0.124	0.081	0.131	1.601	−0.047
		$-1.480^{b,c}$	0.227^{b}	−0.091	0.059	−0.012	−1.486	0.051
2	***experimental***	***1.000***	***0.280***	*n.a.*				
	CASSCF(3,5)	−0.592	0.069	−0.014	0.536		−1.028	n.a.
	NEVPT2(3,5)	−0.792	0.013	−0.014	0.551		−1.343	n.a.
	CASSCF(7,7)	−1.996	0.044	0.063	−0.991		−1.001	n.a.
	NEVPT2(7,7)	−1.929	0.057	0.062	−0.683		−1.246	n.a.
	B3LYP/6-311G	*1.081*	*0.150*	*0.138*	*0.058*	*0.008*	*0.637*	*0.238*
		$-0.946^{b,c}$	0.319^{b}	−0.062	−0.035	0.068	−0.301	−0.616
	BP86/6-311G	0.733	0.132	0.154	0.019	0.053	0.483	0.022
		0.445^{b}	0.234^{b}	0.077	−0.007	0.030	0.323	0.020
	TPSSH/6-311G	−0.831	0.252	−0.124	−0.365	−0.369	0.021	0.006
		$1.096^{b,c}$	0.183^{b}	0.000	0.742	0.662	−0.307	0.000
3	***experimental***	***−0.850***	***0.030***	*n.a.*				
	CASSCF(3,5)	0.469	0.191	−0.011	0.190		0.279	n.a.
	NEVPT2(3,5)	0.344	0.286	−0.011	−0.092		0.436	n.a.
	CASSCF(7,7)	−3.261	0.058	−0.036	−1.043		−2.218	n.a
	NEVPT2(7,7)	−2.996	0.075	−0.036	−0.604		−2.392	n.a.
	B3LYP/6-311G	*−0.948*	*0.048*	*0.003*	*−0.174*	*−0.142*	*−0.271*	*−0.363*
		-1.046^{b}	0.162^{b}	−0.007	−0.214	−0.148	−0.267	−0.408
	BP86/6-311G	-0.289^{c}	0.260	−0.030	0.011	−0.143	−0.185	0.059
		0.233^{b}	0.205^{b}	0.077	0.020	−0.013	0.146	0.002
	TPSSH/6-311G	1.471	0.115	−0.063	−0.056	0.042	1.578	−0.030
		$-1.215^{b,c}$	0.027^{b}	0.074	0.059	−0.061	−1.343	0.054

[a] Unless explicitly indicated, these values were obtained for structural models derived from the experimental crystal structures. [b] Values obtained for structural models derived from geometry optimizations performed at the same level of theory. [c] Although surprising the change in sign is not completely unexpected. For cases such as these, where $E/D \gtrsim 0.2$, the sign of D originates from the competition of two large tensor components; thus, it is more difficult to predict accurately.

show the presence for **1**−**3** of strong covalent interactions between the Mn ions and the supporting ligands.

Predicted Exchange Coupling Constants. The theoretical *J* coupling constants obtained using a broken-symmetry approach and the BP86, B3LYP, and TPSSh functionals, for geometry-optimized and the X-ray structures, are listed in Table 3. With two exceptions, observed for **1** when using the augmented basis sets, BP86 predicts that the superexchange interaction between Mn ions is antiferromagnetic. Although this behavior is consistent with the experimental observations these values are nearly one order of magnitude larger than those observed experimentally. In contrast, the values obtained using B3LYP are of a significantly lower magnitude, with absolute values comparable to those observed experimentally.

However, this functional leads to not only negative (antiferromagnetic coupling) but also to positive (ferromagnetic) coupling constants. While the TPPSh-predicted values for **2** are in good agreement with the experiment, those obtained for **3** are of similar magnitude but of the wrong sign. Surprisingly large, basis-set-dependent changes are observed for the theoretical J values of **1** when using the TPPSh functional. However, this behavior does not seem to be intrinsic to the functional, but rather it is related to the increased difficulty with which geometry-optimized structures are obtained when the size of the basis sets increases.

The interactions which contribute to the antiferromagnetism of dinuclear complexes involve pairs of overlapping "magnetic orbitals" localized on each metal ions. The representative magnetic orbitals for **2** are plotted in Figure 12. Various metal orbitals have very different ability to interact with the bridging atoms, and as a result, their relative importance in transmitting the exchange interactions, measured by the overlap integral[24−29] of the magnetic orbitals, is also very unequal. The overlap integrals of the magnetic orbitals *xz*, *yz*, and *xy* which are presented in Figure 12 are 0.064, 0.057, and 0.010, respectively. This calculation produced a J of -3.2 cm^{-1}.

Predicted ZFSs of Local Metal Sites. We used coupled-perturbed (CP) DFT and CASSCF/NEVPT2 methods as implemented in the quantum chemical software package ORCA to assess the theoretical ZFS parameters and g tensors of local spin sites of **1**−**3**. These results are summarized in Tables 4 and S16a,b. Since the rhombicity of the ZFS tensor, quantified by E/D, is much harder to estimate accurately we focused our discussion on analyzing the axial ZFS parameter D.

Our initial investigations employed heterobinuclear models for which one Mn^{4+} ion was replaced by a diamagnetic Ti^{4+} ion. However, these models led to spurious, difficult to interpret results. Analysis of the time-dependent (TD) DFT results revealed that although in the ground state the titanium site is virtually devoid of unpaired spin density, a sizable number of the lower-energy one-electron vertical excitations involved metal-to-metal charge transfers. Although Retegan et al. have recently described a novel local complete active space configuration interaction (L-CASCI) method to calculate local ZFS tensors of selected sites in polynuclear clusters which does not rely on such a replacement,[67] we used truncated, mononuclear models. Thus, we performed our calculations on models obtained by removing a [MnL′]$^+$ moiety from either the experimental or from the geometry-optimized structures. This procedure led to mononuclear structural models that retained the bridging ligands such that the first coordination sphere of the remaining Mn ion was kept intact.[68]

Inspection of Tables 4 and S16a,b shows that when the computational models used are derived from X-ray crystallographic structures, B3LYP performs well in predicting both the magnitude and the sign of the ZFS parameter D; see Figure S19. For the same models, BP86 exhibits a strong linear correlation with respect to the experimental data; however, the slope is much lower than 1, see Table S20. In contrast, TPPSh performed significantly worse exhibiting essentially no correlation between the theoretical and experimental data sets. These results are analogous to those derived from a systematic investigation of a series of Mn(III) ions.[64] Since TPPSh was shown to be superior to the other two functionals in reproducing superexchagne interactions, hyperfine couplings, and spin state energies including for systems that incorporate manganese(IV) ions this outcome is counter-intuitive.[65] Considering its poor performance in reproducing the ZFSs of Mn(III), Mn(IV) ions, and the g tensors of small radicals, we conclude that TPPSh is poor choice for rationalizing the magnetic properties of **1**−**3**.[69]

The predicted ZFS parameters discussed so far were obtained for computational models derived from experimental structures. However, it is generally preferable to use geometry-optimized, theoretical structures in evaluating spectroscopic parameters. Such structures represent true minima on potential energy surfaces, are of uniform quality, and quite often are the only structures available. Comparison of parameters obtained experimentally, through site-selective spectroscopic methods with theoretical values predicted for geometry-optimized structures, play a crucial role in advancing our understanding of reaction mechanism where intermediates are either short-lived or too reactive to be amenable to crystallographic investigations.[70,71] Thus, developing methods that afford a straightforward correlation between experimental spectroscopic parameters such as ZFSs and theoretical structures remains an important goal.[72] Toward this aim we evaluated the performance of the three functionals under consideration (B3LYP, BP86, and TPPSh), in combination with three, progressively larger, basis sets (6-311G, 6-311G*, and 6-311+G**). When the geometry-optimized structures were used, none of the functional/basis set combinations considered provided a satisfactory description of the ZFSs for all three complexes. Although surprising, these observations are not unprecedented. In particular, the importance of using experimental X-ray structures when assessing theoretical ZFS parameters of polycrystalline samples has been pointed out before.[72,73] In our case, different compounds were better described by different methods. Thus, we observed that the predicted ZFS parameters are nearly independent not only of the basis set used but also of the bridging ligand. These observations suggest that, for geometry-optimized structures, the predicted D values are functional-specific and characteristic of the [L′Mn]$^+$ moiety rather than of the entire complex, that is, they are independent of the bridging ligand. Considering that each functional predicts a distinct electron distribution characterized by a different D value, we speculate that for cases like these in gas phase or for frozen solutions, where intermolecular interactions are weak, D can be used as a diagnostic of the metal ion's oxidation state. We note that a recently reported investigation of Fe- and Mn-corroles arrived at a similar conclusion.[74]

In the sense that the CASSCF/NEVPT2-predicted D values seem to be insensitive to the bridging ligand, our ab initio calculations, on both geometry-optimized and experimental structures, show a behavior analogous to that observed for the CP DFT investigations performed on theoretical structures, see Tables 4 and S16a,b. The CP SCF results obtained for geometry-optimized structures using the BP86 functional are similar to those obtained at the CASSCF/NEVPT2(3,5) level. In contrast, the values obtained using the BP3LYP and TPPSh functionals are comparable with those obtained for the expanded active space, i.e., CASSCF/NEVPT(7,7) and CASSCF/NEVPT(11,9). There are, however, some deviations from this general trend, in particular for CASSCF(3,5), which for **1** and **2** yields a negative value, while for **3** it predicts a positive D value. However, for both **1** and **2** the CASSCF/NEVPT2-predicted $E/D > 0.2$; thus, the sign of D is not reliable. With one exception, BP86 predicts only positive D values of the same magnitude as those predicted for CASSCF/

NEVPT2(3,5). For the latter method the active space is spanned by only the "traditional" set of d-orbitals, that is, the singly occupied, nonbonding t_{2g}-like {xy, xz, yz} orbitals and the virtual, σ-antibonding, e_g*-like set {$x^2 - y^2$, z^2}. Compared to CASSCF/NEVPT(3,5) the active space of CASSCF/NEVPT(7,7) was expanded to include the σ-bonding, doubly occupied, e_g-like orbitals. We have also performed a series of CASSCF/NEVPT(11,9) calculations for which the active space was further increased to incorporate the remaining two molecular orbitals dominated by the frontier orbitals of the R_2NO^- moieties; see Figure S17 and Tables S17−S19. Thus, the active spaces considered here span the 3d orbitals of the Mn ion and the π^*_{NO}, HOMOs of the local R_2NO^- moieties; see Figure S16.

The ground states of **1**−**3** predicted by the CASSCF(3,5) calculations are single-determinantal in nature and correspond to the canonical configuration expected for the pseudo-octahedral d^3, Mn(IV) ions; see Table S17. The extended active space calculations predict multideterminantal ground states which, while still dominated by the canonical configuration (∼50%), also include configurations for which the ligand is redox noninnocent with one unpaired electron localized on one of the NO moieties; see Tables S18 and S19. Consequently, the similarity between the CASSCF/NEVPT2 and the CP DFT calculations also extends to the nature of the predicted ground states such that CASSCF/NEVPT2(3,5) and BP86 yield configurations that are best described considering Mn(IV) ions and diamagnetic ligands and the CASSCF/NEVPT2(7,7), CASSCF/NEVPT2(11,9), B3LYP, and TPSSh predict ground states that can be understood only considering ligands with a strong redox-active character.

Inspection of Table 4 and S16b shows that in most cases the spin−spin contribution to the ZFS tensor, D_{SS}, is small ranging from 0 to 5% of the total D value. However, there are two notable exceptions to this rule. First, for BP86-predicted values the D_{SS} contribution to D ranges from 15 to 33%. Nevertheless, this larger fraction is due, in part, to the fact that while D_{SS} is relatively constant total D values predicted by BP86 are considerably smaller than those predicted by the other methods. Second, the CP DFT, B3LYP/6-311G calculations performed on the X-ray structures of **1** and **2** also predict a D_{SS} that accounts for 12−18% of D. Regardless of the method used to predict ZFSs, the spin−orbit part, D_{SOC}, constitutes the major contribution to the ZFS tensor. Interestingly, D_{SOC} is dominated by $\alpha \rightarrow \beta$ transitions with the second-largest contributions originating from $\alpha \rightarrow \alpha$ and $\beta \rightarrow \beta$ excitations. Both $\alpha \rightarrow \alpha$ and $\alpha \rightarrow \beta$ excitations are dominated by d−d transitions, $\alpha \rightarrow \beta$ excitations account for the contribution of excited doublet states, and $\alpha \rightarrow \alpha$ excitations quantify the contributions of the excited quartet states. The $\beta \rightarrow \beta$ excitations correspond to ligand-to-metal charge transfer and in most cases are negligible. These observations suggest that the spin-conserving contributions to D_{SOC} are dominated by spin-lowering excitations which, in turn, indicate the that crystal field parameter Δ_O, quantifying the splitting of the t_{2g} and e_g* orbitals, is considerably larger than the electron pairing energy P.

Our investigation suggests that for **1**−**3** the local ZFS of can be used as a diagnostic of the redox of the Mn ions and of the terminal tris-hydroxotetraazaadamantane ligands. For **2**, the experimental ZFS was determined with the least amount of ambiguity. In this case, the CASSCF/NEVPT2 and CP DFT (on geometry-optimized structures) predicted ZFS parameters suggest that manganese sites are best described as Mn(IV) ions and that the ligands are redox innocent. In contrast, the experimental ZFSs of **1** and **3** are not as well-established. Nevertheless, the same theoretical methods suggest that exchanging the two alkoxide bridges of **2** with azides for **1** or oxalate for **3** triggers a partial transfer of an electron (per site) from the terminal ligands to the metal ions. We note that neither the CASSCF/NEVPT2 or the CP DFT calculations on theoretical structures provide a satisfactory description of the spectroscopic parameters of all three complexes under investigation. Instead, different compounds were better described by different methods. In this respect, our results are not unprecedented since previous efforts in calculating the ZFS parameters using both DFT and CASSCF for mononuclear Mn(IV) systems were only moderately successful.[75] These studies reinforce the observation that owing to their nondegenerate $^4A_{2g}$ ground states predicting the magnetic properties of genuine pseudo-octahedral Mn(IV) sites is difficult. However, in contrast to the results discussed above, CP DFT calculations on experimental structures showed that B3LYP reproduces not only the magnitude but also the sign of the experimental D values. Since these calculations also predict that the 4,6,10-trihydroxo-3,5,7-trimethyl-1,4,6,10-tetraazaadamantane ligands of **1**−**3** are noninnocent, we conclude that in this case the manganese ions have an increased +3 character.

■ CONCLUSIONS

In conclusion, in this contribution we present a new series of dinuclear Mn^{IV} complexes supported by a terminal 4,6,10-trihydroxo-3,5,7-trimethyl-1,4,6,10-tetraazaadamantane ligand. These three $[Mn^{IV}{}_2]$ compounds incorporate different bridging ligands which, so far, were not reported for Mn^{IV} dimers. Weak magnetic coupling of the Mn^{IV} ions was revealed by studies of the magnetic properties and HF-EPR spectra. The trends in the metal−metal interaction strength were qualitatively confirmed by the "broken symmetry" calculations. The zero-field splitting on Mn(IV) ions was best predicted using CP DFT(B3LYP) performed on models derived the experimental crystal structures. These theoretical investigations revealed that the redox-noninocent character of the tris-hydroxotetraazaadamantane ligand plays a key role in modulating the magnetic properties of these complexes.

■ ASSOCIATED CONTENT

Supporting Information

The Supporting Information is available free of charge at https://pubs.acs.org/doi/10.1021/acs.inorgchem.0c01242.

> Detailed crystallographic information, infrared spectroscopic characterization, electrochemical studies, UVVIS spectra, details of HFEPR interpretations, details of theoretical investigations(PDF)

Accession Codes

CCDC 1867741−1867743 contain the supplementary crystallographic data for this paper. These data can be obtained free of charge via www.ccdc.cam.ac.uk/data_request/cif, or by emailing data_request@ccdc.cam.ac.uk, or by contacting The Cambridge Crystallographic Data Centre, 12 Union Road, Cambridge CB2 1EZ, UK; fax: +44 1223 336033.

AUTHOR INFORMATION

Corresponding Authors

Małgorzata Hołyńska − *Fachbereich Chemie and Wissenschaftliches Zentrum für Materialwissenschaften(WZMW), Philipps-Universität Marburg Hans-Meerwein-Straße, Marburg D-35043, Germany*; Email: holynska@chemie.uni-marburg.de

Andrew Ozarowski − *National High Magnetic Field Laboratory, Florida State University, Tallahassee, Florida 32310, United States*; orcid.org/0000-0001-6225-9796; Email: ozarowsk@magnet.fsu.edu

Sebastian A. Stoian − *Department of Chemistry, University of Idaho, Moscow, Idaho 83844, United States*; orcid.org/0000-0003-3362-7697; Email: sstoian@uidaho.edu

Authors

Dejan Premužić − *Fachbereich Chemie and Wissenschaftliches Zentrum für Materialwissenschaften(WZMW), Philipps-Universität Marburg Hans-Meerwein-Straße, Marburg D-35043, Germany*

Clemens Pietzonka − *Fachbereich Chemie and Wissenschaftliches Zentrum für Materialwissenschaften(WZMW), Philipps-Universität Marburg Hans-Meerwein-Straße, Marburg D-35043, Germany*

Alexander Roseborough − *Department of Chemistry, University of Idaho, Moscow, Idaho 83844, United States*

Complete contact information is available at: https://pubs.acs.org/10.1021/acs.inorgchem.0c01242

Notes

The authors declare no competing financial interest.

ACKNOWLEDGMENTS

This research is funded by DFG HO 5055/3-1 project. The high-field EPR spectra were recorded at the NHMFL, which is funded by the NSF through the Cooperative Agreement No. DMR-1157490 and DMR-1644779, and the State of Florida. Prof. Dr. Stefanie Dehnen and Prof. Dr. Florian Kraus are acknowledged for generous support. SAS acknowledges the support of the University of Idaho. This work used the Extreme Science and Engineering Discovery Environment (through the TG-CHE180015 allocation awarded to S.A.S) which is supported by National Science Foundation grant number ACI-1548562.

REFERENCES

(1) Christou, G. Manganese Carboxylate Chemistry and Its Biological Relevance. *Acc. Chem. Res.* **1989**, *22* (9), 328−335.

(2) Wieghardt, K. The Active Sites in Manganese-Containing Metalloproteins and Inorganic Model Complexes. *Angew. Chem., Int. Ed. Engl.* **1989**, *28* (9), 1153−1172.

(3) Pfxoraro, V. L. Structural Proposals for the Manganese Centers of the Oxygen Evolving Complex: An Inorganic Chemist's Perspective. *Photochem. Photobiol.* **1988**, *48* (2), 249−264.

(4) (a) Bossek, U.; Weyhermueller, T.; Wieghardt, K.; Nuber, B.; Weiss, J. $[L_2Mn_2(\mu\text{-}O)_2(\mu\text{-}O_2)](ClO_4)_2$. The First Binuclear ($\mu$-peroxo)dimanganese(IV) Complex (L = 1,4,7-Trimethyl-1,4,7-Triazacyclononane). A Model for the $S_4 \rightarrow S_0$ Transformation in the Oxygen-Evolving Complex in Photosynthesis. *J. Am. Chem. Soc.* **1990**, *112* (17), 6387−6388. (b) Mukherjee, S.; Stull, J. A.; Yano, J.; Stamatatos, T. C.; Pringouri, K.; Stich, T. A.; Abboud, K. A.; Britt, R. D.; Yachandra, V. K.; Christou, G. Synthetic Model of the Asymmetric [Mn_3CaO_4] Cubane Core of the Oxygen-Evolving Complex of Photosystem II. *Proc. Natl. Acad. Sci. U. S. A.* **2012**, *109* (7), 2257−2262.

(5) Cotruvo, J. A.; Stich, T. A.; Britt, R. D.; Stubbe, J. Mechanism of Assembly of the Dimanganese-Tyrosyl Radical Cofactor of Class Ib Ribonucleotide Reductase: Enzymatic Generation of Superoxide Is Required for Tyrosine Oxidation via a Mn(III)Mn(IV) Intermediate. *J. Am. Chem. Soc.* **2013**, *135* (10), 4027−4039.

(6) Cox, N.; Retegan, M.; Neese, F.; Pantazis, D. A.; Boussac, A.; Lubitz, W. Photosynthesis. Electronic Structure of the Oxygen-Evolving Complex in Photosystem II prior to O-O Bond Formation. *Science* **2014**, *345* (6198), 804−808.

(7) Wu, X.; Seo, M. S.; Davis, K. M.; Lee, Y.-M.; Chen, J.; Cho, K.-B.; Pushkar, Y. N.; Nam, W. A. Highly Reactive Mononuclear Non-Heme Manganese(IV)-Oxo Complex That Can Activate the Strong C-H Bonds of Alkanes. *J. Am. Chem. Soc.* **2011**, *133*, 20088−20091.

(8) Massie, A. A.; Denler, M. C.; Cardoso, L. T.; Walker, A. N.; Hossain, M. K.; Day, V. W.; Nordlander, E.; Jackson, T. A. Equatorial Ligand Perturbations Influence the Reactivity of Manganese(IV)-Oxo Complexes. *Angew. Chem., Int. Ed.* **2017**, *56*, 4178−4182.

(9) Rice, D. B.; Massie, A. A.; Jackson, T. A. Experimental and Multireference ab Initio Investigations of Hydrogen-Atom-Transfer Reactivity of a Mononuclear Mn^{IV}-oxo Complex. *Inorg. Chem.* **2019**, *58*, 13902−13916.

(10) Lee, Y.; Jackson, T. A. Ligand Influence on Structural Properties and Reactivity of Bis(μ-oxo)dimanganese(III,IV) Species and Comparison of reactivity with Terminal Mn^{IV}-oxo Complexes. *ChemistrySelect* **2018**, *3*, 13507−13516.

(11) Berggren, G.; Thapper, A.; Huang, P.; Eriksson, L.; Styring, S.; Anderlund, M. F. Mechanistic Studies on the Water-Oxidizing Reaction of Homogeneous Manganese-Based Catalysts: Isolation and Characterization of a Suggested Catalytic Intermediate. *Inorg. Chem.* **2011**, *50* (8), 3425−3430.

(12) Mukherjee, S.; Weyhermüller, T.; Bothe, E.; Wieghardt, K.; Chaudhuri, P. Dinuclear and mononuclear manganese(IV)-radical complexes and their catalytic catecholase activity. *Dalton Trans.* **2004**, 3842−3853.

(13) (a) Caudle, M. T.; Kampf, J. W.; Kirk, M. L.; Rasmussen, P. G.; Pecoraro, V. L. The First Binuclear Mn(IV) Complex Containing a Bridging Imidazolate Ligand Exhibits Unique EPR Spectral Features. *J. Am. Chem. Soc.* **1997**, *119*, 9297−9298. (b) Burdinski, D.; Bill, E.; Birkelbach, F.; Wieghardt, K.; Chaudhuri, P. Long-Range Exchange Interactions and Integer-Spin $S_t = 2$ EPR Spectra of a $Cr^{III}Zn^{II}Cr^{III}$ Species with Multiplet Mixing. *Inorg. Chem.* **2001**, *40*, 1160−1166. (c) Baldwin, M. J.; Stemmler, T. L.; Riggs-Gelasco, P. J.; Kirk, M. L.; Penner-Hahn, J. E.; Pecoraro, V. L. Structural and Magnetic Effects of Successive Protonations of Oxo Bridges in High-Valent Manganese Dimers. *J. Am. Chem. Soc.* **1994**, *116*, 11349−11356.

(14) Duboc-Toia, C.; Hummel, H.; Bill, E.; Barra, A.-L.; Chouteau, G.; Wieghardt, K. Integer-Spin Multifrequency EPR Spectroscopy of a Ferromagnetically Coupled, Oxo-Bridged $Mn^{IV}Mn^{IV}$ Model Complex. *Angew. Chem., Int. Ed.* **2000**, *39* (16), 2888−2890.

(15) Torayama, H.; Asada, H.; Fujiwara, M.; Matsushita, T. Structures and Properties of Di-μ-Oxodimanganese(IV) Complexes with Bidentate Schiff Bases, N-Alkyl-Substituted-Salicylideneamine. *Polyhedron* **1998**, *17* (22), 3859−3874. Torayama, H.; Nishide, T.; Asada, H.; Fujiwara, M.; Matsushita, T. Preparation and Characterization of Different Two Types of Di-μ-Oxodimanganese(IV) Complexes with Tetradentate Schiff Bases. *Polyhedron* **1998**, *17* (1), 105−118.

(16) (a) Samoľová, E.; Premužić, D.; Plociennik, S.; Hołyńska, M. Bis(Benzimidazole) as Supramolecular Building Block in Manganese-(IV) Chemistry. *J. Mol. Struct.* **2019**, *1176*, 366−375. (c) Goldcamp, M. J.; Krause, J. A.; Bauer; Baldwin, M. J. Structural Characterization of a Zinc(II) Complex of a Tris(Oxime)Amine Ligand. *J. Chem. Crystallogr.* **2005**, *35* (1), 77−83. (d) Premužić, D.; Korabik, M.; Hołyńska, M. Structure and Magnetic Properties of a New Binuclear Copper(II) Complex of a Tripodal Oxime. *J. Mol. Struct.* **2014**, *1059*, 265−270. (e) Roseborough, A.; Wheeler, K. A.; Hołyńska, H.; Stoian, S. A. Synthesis and Electronic Structure of a Mononuclear Copper(II)

Complex Supported by Tris(2-hydroxyliminopropyl)amine. *Polyhedron* **2020**, *177*, 114306.

(17) Semakin, A. N.; Sukhorukov, A. Y.; Lesiv, A. V.; Ioffe, S. L.; Lyssenko, K. A.; Nelyubina, Y. V.; Tartakovsky, V. A. Unusual Intramolecular Cyclization of Tris(β-Oximinoalkyl)amines. The First Synthesis of 1,4,6,10-Tetraazaadamantanes. *Org. Lett.* **2009**, *11* (18), 4072−4075.

(18) Premužić, D.; Muche, S.; Hołyńska, M. Unprecedented Non-Cytotoxic [$\mathrm{Co^{III}}_4\mathrm{Ln^{III}}$]-Core Complexes with a Tripodal Oxime Ligand − Synthesis, Structure, Properties and Potential Applications. *New J. Chem.* **2014**, *38* (7), 2894−2901.

(19) (a) König, E. *Magnetic Properties of Coordination and Organometallic Transition Metal Compounds*; Hellwege, K.-H., Hellwege, A. M., Eds.; Springer: Berlin,1966; pp 27−29. (b) Bain, G. A.; Berry, J. F. Diamagnetic Corrections and Pascal's Constants. *J. Chem. Educ.* **2008**, *85* (4), 532−536.

(20) Hassan, A. K.; Pardi, L. A.; Krzystek, J.; Sienkiewicz, A.; Goy, P.; Rohrer, M.; Brunel, L.-C. Ultrawide Band Multifrequency High-Field EMR Technique: A Methodology for Increasing Spectroscopic Information. *J. Magn. Reson.* **2000**, *142* (2), 300−312.

(21) Sheldrick, G. M. Crystal structure refinement with SHELXL. *Acta Crystallogr., Sect. C: Struct. Chem.* **2015**, *C71*, 3−8.

(22) Frisch, M. J.; Trucks, G. W.; Schlegel, H. B.; Scuseria, G. E.; Robb, M. A.; Cheeseman, J. R.; Scalmani, G.; Barone, V.; Mennucci, B.; Petersson, G. A.; Nakatsuji, H.; Caricato, M.; Li, X.; Hratchian, H. P.; Izmaylov, A. F.; Bloino, J.; Zheng, G.; Sonnenberg, J. L.; Hada, M.; Ehara, M.; Toyota, K.; Fukuda, R.; Hasegawa, J.; Ishida, M.; Nakajima, T.; Honda, Y.; Kitao, O.; Nakai, H.; Vreven, T.; Montgomery, J. A., Jr.; Peralta, J. E.; Ogliaro, F.; Bearpark, M.; Heyd, J. J.; Brothers, E.; Kudin, K. N.; Staroverov, V. N.; Kobayashi, R.; Normand, J.; Raghavachari, K.; Rendell, A.; Burant, J. C.; Iyengar, S. S.; Tomasi, J.; Cossi, M.; Rega, N.; Millam, J. M.; Klene, M.; Knox, J. E.; Cross, J. B.; Bakken, V.; Adamo, C.; Jaramillo, J.; Gomperts, R.; Stratmann, R. E.; Yazyev, O.; Austin, A. J.; Cammi, R.; Pomelli, C.; Ochterski, J. W.; Martin, R. L.; Morokuma, K.; Zakrzewski, V. G.; Voth, G. A.; Salvador, P.; Dannenberg, J. J.; Dapprich, S.; Daniels, A. D.; Farkas, O.; Foresman, J. B.; Ortiz, J. V.; Cioslowski, J.; Fox, D. J. *Gaussian 09*, revision E.01; Gaussian, Inc.: Wallingford, CT, 2009.

(23) (a) Neese, F. *ORCA - An Ab Initio, Density Functional and Semiempirical Program Package*, version 4.0.1; Surf Sara: Amsterdam, 2017. (b) Neese, F. The ORCA Program System. *Wiley Interdiscip. Rev.: Comput. Mol. Sci.* **2012**, *2* (1), 73−78.

(24) Noodleman, L. Valence Bond Description of Antiferromagnetic Coupling in Transition Metal Dimers. *J. Chem. Phys.* **1981**, *74* (10), 5737−5743.

(25) Noodleman, L.; Davidson, E. R. Ligand Spin Polarization and Antiferromagnetic Coupling in Transition Metal Dimers. *Chem. Phys.* **1986**, *109* (1), 131−143.

(26) Noodleman, L.; Case, D. A. Density-Functional Theory of Spin Polarization and Spin Coupling in Iron—Sulfur Clusters. *Adv. Inorg. Chem.* **1992**, *38*, 423−458.

(27) Malrieu, J. P.; Caballol, R.; Calzado, C. J.; de Graaf, C.; Guihéry, N. Magnetic Interactions in Molecules and Highly Correlated Materials: Physical Content, Analytical Derivation, and Rigorous Extraction of Magnetic Hamiltonians. *Chem. Rev.* **2014**, *114* (1), 429−492.

(28) Onofrio, N.; Mouesca, J.-M. Analysis of the Singlet−Triplet Splitting Computed by the Density Functional Theory−Broken-Symmetry Method: Is It an Exchange Coupling Constant? *Inorg. Chem.* **2011**, *50* (12), 5577−5586.

(29) Rodríguez-Fortea, A.; Alemany, P.; Alvarez, S.; Ruiz, E. Exchange Coupling in Halo-Bridged Dinuclear Cu(II) Compounds: A Density Functional Study. *Inorg. Chem.* **2002**, *41* (14), 3769−3778.

(30) Schäfer, A.; Horn, H.; Ahlrichs, R. Fully Optimized Contracted Gaussian Basis Sets for Atoms Li to Kr. *J. Chem. Phys.* **1992**, *97* (4), 2571−2577.

(31) Ahlrichs, R. et al., unpublished.

(32) The Ahlrichs auxiliary basis sets (https://www.basissetexchange.org/) have been hardwired into the ORCA software.

(33) Eichkorn, K.; Treutler, O.; Öhm, H.; Häser, M.; Ahlrichs, R. Auxiliary Basis Sets to Approximate Coulomb Potentials. *Chem. Phys. Lett.* **1995**, *240* (4), 283−290.

(34) Eichkorn, K.; Weigend, F.; Treutler, O.; Ahlrichs, R. Auxiliary Basis Sets for Main Row Atoms and Transition Metals and Their Use to Approximate Coulomb Potentials. *Theor. Chem. Acc.* **1997**, *97* (1−4), 119−124.

(35) Becke, A. D. Density-Functional Exchange-Energy Approximation with Correct Asymptotic Behavior. *Phys. Rev. A: At., Mol., Opt. Phys.* **1988**, *38* (6), 3098−3100.

(36) Perdew, J. P. Density-Functional Approximation for the Correlation Energy of the Inhomogeneous Electron Gas. *Phys. Rev. B: Condens. Matter Mater. Phys.* **1986**, *33* (12), 8822−8824.

(37) Perdew, J. P. Erratum: Density-Functional Approximation for the Correlation Energy of the Inhomogeneous Electron Gas. *Phys. Rev. B: Condens. Matter Mater. Phys.* **1986**, *34* (10), 7406−7406.

(38) Kendall, R. A.; Früchtl, H. A. The Impact of the Resolution of the Identity Approximate Integral Method on Modern Ab Initio Algorithm Development. *Theor. Chem. Acc.* **1997**, *97* (1−4), 158−163.

(39) Roos, B. O.; Taylor, P. R.; Sigbahn, P. E. M. A complete active space SF method (CASSCF) using a density matrix formulated super-CI approach. *Chem. Phys.* **1980**, *48*, 157−173.

(40) Angeli, C.; Cimiraglia, R.; Evangelisti, S.; Leininger, T.; Malrieu, J.-P. Introduction of n-electron valence states for multi-reference perturbation theory. *J. Chem. Phys.* **2001**, *114*, 10252−10264.

(41) Neese, F. Calculation of the zero-field splitting tensor on the basis of hybrid density functional and Hartree-Fock theory. *J. Chem. Phys.* **2007**, *127*, 164112.

(42) Weigend, F.; Ahlrichs, R. Balanced basis sets of split valence, triple zeta valence and quadruple zeta valence quality for H to Rn: Design and assessment of accuracy. *Phys. Chem. Chem. Phys.* **2005**, *7*, 3297−3305.

(43) Weigend, F. Hatree-Fock Exchange Fitting Basis Sets for H to Rn. *J. Comput. Chem.* **2008**, *29*, 167−175.

(44) Hosseini-Monfared, H.; Bikas, R.; Sanchiz, J.; Lis, T.; Siczek, M.; Tucek, J.; Zboril, R.; Mayer, P. Syntheses, Structures and Magnetic Properties of Azido- and Phenoxo-Bridged Complexes of Manganese Containing Tridentate Aroylhydrazone Based Ligands. *Polyhedron* **2013**, *61*, 45−55.

(45) Ge, C.-H.; Cui, A.-L.; Ni, Z.-H.; Jiang, Y.-B.; Zhang, L.-F.; Ribas, J.; Kou, H.-Z. $\mu_{1,1}$-Azide-Bridged Ferromagnetic $\mathrm{Mn^{III}}$ Dimer with Slow Relaxation of Magnetization. *Inorg. Chem.* **2006**, *45* (13), 4883−4885.

(46) Berg, N.; Rajeshkumar, T.; Taylor, S. M.; Brechin, E. K.; Rajaraman, G.; Jones, L. F. What Controls the Magnetic Interaction in Bis-μ-Alkoxo $\mathrm{Mn^{III}}$ Dimers? A Combined Experimental and Theoretical Exploration. *Chem. - Eur. J.* **2012**, *18* (19), 5906−5918.

(47) Fuller, A. L.; Watkins, R. W.; Dunbar, K. R.; Prosvirin, A. V.; Arif, A. M.; Berreau, L. M. Manganese(II) Chemistry of a New N_3O-Donor Chelate Ligand: Synthesis, X-Ray Structures, and Magnetic Properties of Solvent- and Oxalate-Bound Complexes. *Dalt. Trans.* **2005**, 1891−1896.

(48) Glerup, J.; Goodson, P. A.; Hodgson, D. J.; Michelsen, K. Magnetic Exchange through Oxalate Bridges: Synthesis and Characterization of (μ-Oxalato)dimetal(II) Complexes of Manganese, Iron, Cobalt, Nickel, Copper, and Zinc. *Inorg. Chem.* **1995**, *34* (25), 6255−6264.

(49) (a) Semenaka, V. V.; Nesterova, O. V.; Kokozay, V. N.; Dyakonenko, V. V.; Zubatyuk, R. I.; Shishkin, O. V.; Boča, R.; Jezierska, J.; Ozarowski, A. $\mathrm{Cr^{III}} - \mathrm{Cr^{III}}$ Interactions in Two Alkoxo-Bridged Heterometallic $\mathrm{Zn_2Cr_2}$ Complexes Self-Assembled from Zinc Oxide, Reinecke's Salt, and Diethanolamine. *Inorg. Chem.* **2010**, *49* (12), 5460−5471. (b) Riesen, H.; Gudel, H. U. Exchange Interactions in a Trigonal Chromium(III) Pair: Optical Spectroscopy of Tris-(μ-Hydroxo)-Bis-[(1,4,7-trimethyl-1,4,7-Triazacyclononane) chromium-(III)] triperchlorate. *Mol. Phys.* **1987**, *60*, 1221−1244. (c) Kremer, S. EPR spectroscopic study of S = 1, 2, and 3 spin states of tris(.mu.-

hydroxo)-bridged chromium(III) dimers. *Inorg. Chem.* **1985**, *24*, 887−890. (d) Morsing, T. J.; Weihe, H.; Bendix, J. Probing Effective Hamiltonian Operators by Single-Crystal EPR: A Case Study Using Dinuclear Cr(III) Complexes. *Inorg. Chem.* **2016**, *55* (4), 1453−1460. (e) Glerup, J.; Goodson, P.; Hodgson, D. J.; Masood, M. A.; Michelsen, K. Syntheses and characterization of novel binuclear chromium (III) complexes of 1,4,8,11-tetraazacyclotetradecane (cyclam). *Inorg. Chim. Acta* **2005**, *358*, 295−302.

(50) (a) Bencini, A.; Gatteschi, D. In *EPR of Exchange Coupled Systems*; Springer Verlag: Berlin/Heidelberg, 1990. (b) Abragam, A.; Bleaney, B. In *Electron Paramagnetic Resonance of Transition Ions*; Clarendon Press: London, 1970. (c) Owen, J. Paramagnetic Resonance Measurements of Exchange Interactions. *J. Appl. Phys.* **1961**, *32* (3), S213−S217. (d) Boča, R. In *Theoretical Foundations of Molecular Magnetism*; Elsevier: Amsterdam, 1999. (e) Boča, R. Zero-Field Splitting in Metal Complexes. *Coord. Chem. Rev.* **2004**, *248* (9−10), 757−815.

(51) Okamura, M. Y.; Hoffman, B. M. Electron Spin Resonance of the Thermally Excited Quintet State of an Oxo-Bridged Binuclear Iron(III) Complex. *J. Chem. Phys.* **1969**, *51* (7), 3128−3129. Ozarowski, A.; McGarvey, B. R.; Drake, J. E. EPR Study of $S = 2$ and $S = 3$ States of Fe-O-Fe Dimers in $Na_4[Fe(edta)]_2O \cdot 3\ H_2O$ and $\{[Fe(phen)_2]_2O\}(NO_3)_4 \cdot 7\ H_2O$. X-Ray Structure Determination of $Na_4[Fe(edta)]_2O \cdot 3\ H_2O$. *Inorg. Chem.* **1995**, *34* (22), 5558−5566. Holgate, S. J. W.; Bondarenko, G.; Collison, D.; Mabbs, F. E. Single Crystal EPR Studies of $[enH_2][\{Fe(HEDTA)\}_2O]{\cdot}6\ H_2O$ [en = Ethylenediamine; HEDTA = N-Hydroxyethylethylenediaminetriacetate$^{(3-)}$]. *Inorg. Chem.* **1999**, *38* (10), 2380−2385. ter Heerdt, P.; Stefan, M.; Goovaerts, E.; Caneschi, A.; Cornia, A. Single-Ion and Molecular Contributions to the Zero-Field Splitting in an iron(III)-Oxo Dimer Studied by Single Crystal W-Band EPR. *J. Magn. Reson.* **2006**, *179* (1), 29−37.

(52) Tran, B. L.; Krzystek, J.; Ozarowski, A.; Chen, C.-H.; Pink, M.; Karty, J. A.; Telser, J.; Meyer, K.; Mindiola, D. J. Formation and Reactivity of the Terminal Vanadium Nitride Functionality. *Eur. J. Inorg. Chem.* **2013**, *2013* (22−23), 3916−3929.

(53) Carr, S. G.; Smith, T. D.; Pilbrow, J. R. Electron Spin Resonance Study of Paramagnetic Ion Pair Systems with Non-Parallel Alignment of Their Axes. *J. Chem. Soc., Faraday Trans. 2* **1974**, *70*, 497−511.

(54) Maurice, R.; Sivalingam, K.; Ganyushin, D.; Guihéry, N.; de Graaf, C.; Neese, F. Theoretical Determination of the Zero-Field Splitting in Copper Acetate Monohydrate. *Inorg. Chem.* **2011**, *50* (13), 6229−6236.

(55) Ozarowski, A. The Zero-Field-Splitting Parameter D in Binuclear Copper(II) Carboxylates Is Negative. *Inorg. Chem.* **2008**, *47* (21), 9760−9762.

(56) Ozarowski, A.; Calzado, C. J.; Sharma, R. P.; Kumar, S.; Jezierska, J.; Angeli, C.; Spizzo, F.; Ferretti, V. Metal−Metal Interactions in Trinuclear Copper(II) Complexes $[Cu_3(RCOO)_4(H_2TEA)_2]$ and Binuclear $[Cu_2(RCOO)_2(H_2TEA)_2]$. Syntheses and Combined Structural, Magnetic, High-Field Electron Paramagnetic Resonance, and Theoretical Studies. *Inorg. Chem.* **2015**, *54* (24), 11916−11934.

(57) Aromi, G.; Telser, J.; Ozarowski, A.; Brunel, L. C.; Stoeckli-Evans, H. M.; Krzystek, J. Synthesis, Crystal Structure, and High Precision High-Frequency and -Field Electron Paramagnetic Resonance Investigation of a Mn(III) Complex: $[Mn(dbm)_2(py)_2](ClO_4)$. *Inorg. Chem.* **2005**, *44*, 187−196.

(58) Zlatar, M.; Gruden, M.; Vassilyeva, O. Y.; Buvaylo, E. A.; Ponomarev, A. N.; Zvyagin, S. A.; Wosnitza, J.; Krzystek, J.; Garcia-Fernandez, P.; Duboc, C. Origin of the Zero-Field Splitting in Mononuclear Octahedral Mn^{IV} Complexes: A Combined Experimental and Theoretical Investigation. *Inorg. Chem.* **2016**, *55* (3), 1192−1201.

(59) Brion, H.; Moser, C.; Yamazaki, M. Electronic Structure of Nitric Oxide. *J. Chem. Phys.* **1959**, *30*, 673−681.

(60) Bentley, J.; Madden, K. P. Theoretical Investigation of Spin-Trapping Reactions. *J. Am. Chem. Soc.* **1994**, *116*, 11397−11406.

(61) Beck, R.; Nibler, J. W. ESR Studies and HMO Calculations on Benzosemiquinone Radical Anions: a Physical Chemistry Experiments. *J. Chem. Educ.* **1989**, *66*, 263−266.

(62) Weil, J. A.; Bolton, J. R. *Electron Paramagnetic Resonance Elementary Theory and Practical Applications*, 2nd ed.; Wiley-Interscience, John Wiley & Sons, Inc.: Hoboken, NJ, 2007.

(63) Koch, W.; Holthausen, M. C. *A Chemist's Guide to Density Functional Theory*, 2nd ed.; Wiley-VCH: Weinheim, 2001.

(64) Duboc, C.; Ganyushin, D.; Sivalingam, K.; Collomb, M.-N.; Neese, F. Systematic Theoretical Study of the Zero-Field Splitting in Coordination Complexes of Mn(III). Density Functional Theory versus Multireference Wave Function Approaches. *The. J. Phys. Chem. A* **2010**, *114* (39), 10750−10758.

(65) Orio, M.; Pantazis, D. A.; Petrenko, T.; Neese, F. Magnetic and Spectroscopic Properties of Mixed Valence Manganese(III,IV) Dimers: A Systematic Using Broken Symmetry Density Functional Theory. *Inorg. Chem.* **2009**, *48*, 7251−7260.

(66) Jensen, K. P. Bioinorganic Chemistry Modeled with the TPSSh Density Functional. *Inorg. Chem.* **2008**, *47* (22), 10357−10365.

(67) Retegan, M.; Cox, N.; Pantazis, D. A.; Neese, F. A First-Principles Approach to the Calculation of the on-Site Zero-Field Splitting in Polynuclear Transition Metal Complexes. *Inorg. Chem.* **2014**, *53* (21), 11785−11793.

(68) Retegan, M.; Collomb, M.-N.; Neese, F.; Duboc, C. A combined high-field EPR and quantum chemical study on a weakly ferromagnetically coupled dinuclear Mn(III) complex. A complete analysis of the EPR spectrum beyond the strong coupling limit. *Phys. Chem. Chem. Phys.* **2013**, *15*, 223−234.

(69) Gauss, J.; Kállay, M.; Neese, F. Calculation of Electronic *g* -Tensors Using Coupled Cluster Theory †. *J. Phys. Chem. A* **2009**, *113* (43), 11541−11549.

(70) Snyder, B. E. R.; Bols, M. L.; Schoonheydt, R. A.; Sels, B. F.; Solomon, E. I. Iron and Copper Active Sites in Zeolites and Their Correlation to Metalloenzymes. *Chem. Rev.* **2018**, *118* (5), 2718−2768.

(71) Jasniewski, A. J.; Que, L. Dioxygen Activation by Nonheme Diiron Enzymes: Diverse Dioxygen Adducts, High-Valent Intermediates, and Related Model Complexes. *Chem. Rev.* **2018**, *118* (5), 2554−2592.

(72) Duboc, C.; Phoeung, T.; Zein, S.; Pécaut, J.; Collomb, M.-N.; Neese, F. Origin of the Zero-Field Splitting in Mononuclear Octahedral Dihalide Mn^{II} Complexes: An Investigation by Multi-frequency High-Field Electron Paramagnetic Resonance and Density Functional Theory. *Inorg. Chem.* **2007**, *46* (12), 4905−4916.

(73) Zein, S.; Neese, F. Ab Initio and Coupled-Perturbed Density Functional Theory Estimation of Zero-Field Splittings in Mn ^{II} Transition Metal Complexes. *J. Phys. Chem. A* **2008**, *112* (34), 7976−7983.

(74) Krzystek, J.; Schnegg, A.; Aliabadi, A.; Holldack, K.; Stoian, S. A.; Ozarowski, A.; Hicks, S. D.; Abu-Omar, M. M.; Thomas, K. E.; Ghosh, A.; et al. Advanced Paramagnetic Resonance Studies on Manganese and Iron Corroles with a Formal d^4 Electron Count. *Inorg. Chem.* **2020**, *59* (2), 1075−1090.

(75) Leto, D. F.; Massie, A. A.; Colmer, H. E.; Jackson, T. A. X-Band Electron Paramagnetic Resonance Comparison of Mononuclear Mn^{IV}-Oxo and Mn^{IV}-Hydroxo Complexes and Quantum Chemical Investigation of Mn^{IV} Zero-Field Splitting. *Inorg. Chem.* **2016**, *55* (7), 3272−3282.